Tectonophysics 890 (2024) 230497

Contents lists available at ScienceDirect

Tectonophysics

journal homepage: www.elsevier.com/locate/tecto

Rate-and-state friction of epidote gouge under hydrothermal conditions and implications for the stability of subducting faults under greenschist metamorphic conditions

Mengke An [a,b], Zhenyu Yin [a,*], Fengshou Zhang [c,*], Rui Huang [c], Derek Elsworth [b,d]

[a] Department of Civil and Environmental Engineering, The Hong Kong Polytechnic University, Hung Hom, Kowloon, Hong Kong 100872, China
[b] Department of Energy and Mineral Engineering, EMS Energy Institute and G3 Center, The Pennsylvania State University, University Park, PA 16802, USA
[c] Department of Geotechnical Engineering, College of Civil Engineering, Tongji University, Shanghai 200092, China
[d] Department of Geosciences, The Pennsylvania State University, University Park, PA 16802, USA

ARTICLE INFO

Keywords:
Subduction faults
Epidote gouge
Greenschist metamorphism
Rate-and-state friction
Fault stability transition

ABSTRACT

Epidote is a common hydrous mineral present in subduction zones subject to greenschist metamorphic conditions – and potentially an important control on the fault stability-instability transition observed under greenschist facies. We explore controls on this transition through shear experiments on simulated epidote gouge at temperatures of 100–500 °C, effective normal stresses of 100–300 *MPa* and pore fluid pressures of 30–75 *MPa*. We use rate-and-state friction to define these controls of temperature, effective stress and pore fluid pressure on gouge stability. Experimental results indicate that the epidote gouge is frictionally strong ($\mu \sim 0.73$) and the frictional strength is insensitive to variations in temperature or pressure. With increasing temperature, the epidote gouge exhibits a first transition from velocity-strengthening to velocity-weakening at sub-greenschist conditions ($T < 100$ °C) before transitioning to velocity-strengthening under greenschist metamorphic conditions ($T > 300$ °C). Elevating the pore fluid pressure or decreasing the effective stress promotes unstable sliding. The transition in gouge rheology at varied temperatures and pressures is explained by the competition between granular flow-induced gouge dilation and pressure solution-induced gouge compaction. Our results demonstrate that the rate-and-state frictional stability of epidote gouges support the potential for a fault stability-instability-stability transition for subduction under greenschist metamorphic conditions.

1. Introduction

Dehydration of a variety of hydrous minerals (e.g., chlorite, zoisite/epidote, glaucophane, lawsonite, talc, serpentine and amphibole) in subduction zones may produce copious volumes of released water (Forneris and Holloway, 2003; Oliver, 1996; Pawley et al., 1996; Peacock and Hyndman, 1999; Schmidt and Poli, 1998). These dehydration products will elevate pore fluid pressures and reduce effective stresses, contributing to dehydration embrittlement in the subducting slab where the excess pore fluids are unable to drain (Deseta et al., 2014; Hacker et al., 2003; Incel et al., 2017; John et al., 2009; Jung et al., 2004). Previous studies demonstrate that such dehydration embrittlement may trigger upper plate earthquakes in the subducting oceanic crust (Green II and Houston, 1995; Hacker et al., 2003; Kirby, 1995; Raleigh, 1967; Spinelli and Wang, 2009). Consequently, a systematic study of the physical and mechanical properties of the hydrous minerals under subduction temperatures and pressures, is warranted as a key prerequisite for understanding fault deformation, seismic triggering and geodynamic processes in subduction zones (Ando et al., 2012; Behr et al., 2018; Fagereng and Toy, 2011; Tulley et al., 2022).

Extensive laboratory studies have explored the frictional strength and stability of hydrous mineral gouges under pressure and temperature conditions relevant to subduction zones. These include chlorite (Belzer and French, 2022; Okamoto et al., 2019), blueschist (glaucophane-lawsonite mixtures) (Sawai et al., 2016), talc (Boneh and Hirth, 2023; Moore and Lockner, 2008), serpentine (Reinen et al., 1994; Tesei et al., 2018), and amphibole gouges (Liu and He, 2020) – however, few examine the response of epidote gouges and especially at high temperatures (An et al., 2021; Fagereng and Ikari, 2020; Kolawole et al., 2019). Epidote is characteristic of other hydrous Ca-Al-silicate mineral, with

* Corresponding authors.
E-mail addresses: zhenyu.yin@polyu.edu.hk (Z. Yin), fengshou.zhang@tongji.edu.cn (F. Zhang).

https://doi.org/10.1016/j.tecto.2024.230497
Received 25 April 2024; Received in revised form 29 August 2024; Accepted 2 September 2024
Available online 3 September 2024

the chemical formula of $Ca_2Al_{3-x}Fe_x(SiO_4)(Si_2O_7)O(OH)$. It is commonly generated under greenschist, blueschist and epidotite-amphibolite metamorphic conditions and widely distributed in metabasites, metapelites, and metacherts within subducting plates (Bird and Spieler, 2004; Chen et al., 2019; Enami et al., 2004; Franz and Liebscher, 2004; Wehrens et al., 2016). In retrograde faults exhuming mafic rocks, the epidote mineral also occurs as a result of retrograde greenschist metamorphism (Diener et al., 2016; Fagereng and Diener, 2011; Fagereng and Ikari, 2020).

Epidote minerals generally contain ~2 *wt*% bound water in their crystal structures and typically comprise up to one fifth by weight of subducting mid-ocean ridge basalts (MORB) (Apted and Liou, 1983; Frei et al., 2004; Schmidt and Poli, 1998). Consequently, the dehydration reaction injects a significant mass of water into the subducting slab and thus, potentially, the mantle (Hu et al., 2017; Li et al., 2021; Spandler et al., 2003). An important question arises as to whether epidote-filled faults in the subducting slab would show stable or unstable sliding behaviors upon fluid pressurization. Current experimental observations are limited to temperatures representative only of the shallow crust (An et al., 2021; Fagereng and Ikari, 2020; Shads 4–1 sample in Kolawole et al., 2019), highlighting the need for measurements of rheology at high temperatures and pressures – in particular at the fluid pressurization conditions upon dehydration reactions that could affect the porosity and elastic mechanical properties in the mineral skeleton and further induce strain localization and shear instabilities during deformation (Brantut et al., 2011a, 2011b, 2012).

Spring-slider models are commonly used to simulate the stability response of tectonic loading and failure that may contribute to seismicity on faults (Fig. 1a) (Gu et al., 1984; Marone, 1998). Fault rupture initiates when the resultant shear stress on the pre-existing fault plane exceeds the frictional resistance. From Amonton's law, the strength failure criterion is defined and the resultant shear stress τ is expressed as,

$$\tau = C_0 + \mu \bullet (\sigma_n - P_f) = C_0 + \mu \bullet \sigma_{neff} \quad (1)$$

where C_0 represents the cohesive strength, μ is the coefficient of friction, σ_n, P_f, and σ_{neff} indicate the normal stress, pore fluid pressure and effective normal stress, respectively. Eq. (1) denotes the stress condition when a fault would slip, but it cannot define the slip velocity for a fault rupture. The evolution of fault friction with slip velocity may be represented by the empirical rate-and-state friction (RSF) law (Dieterich, 1979; Marone, 1998; Rice, 1983; Rice and Ruina, 1983; Ruina, 1983; Schloz, 2002). RSF theory accommodates the variation of coefficient of friction with change in slip velocity and the evolution of contact area under an applied effective stress. A variety of expressions describe RSF theory with the most frequently employed written as,

$$\mu = \mu_0 + a\ln\left(\frac{V}{V_0}\right) + b\ln\left(\frac{V_0\theta}{D_c}\right) \quad (2)$$

$$\frac{d\theta}{dt} = 1 - \frac{V\theta}{D_c} \text{ (slowness law)} \quad (3)$$

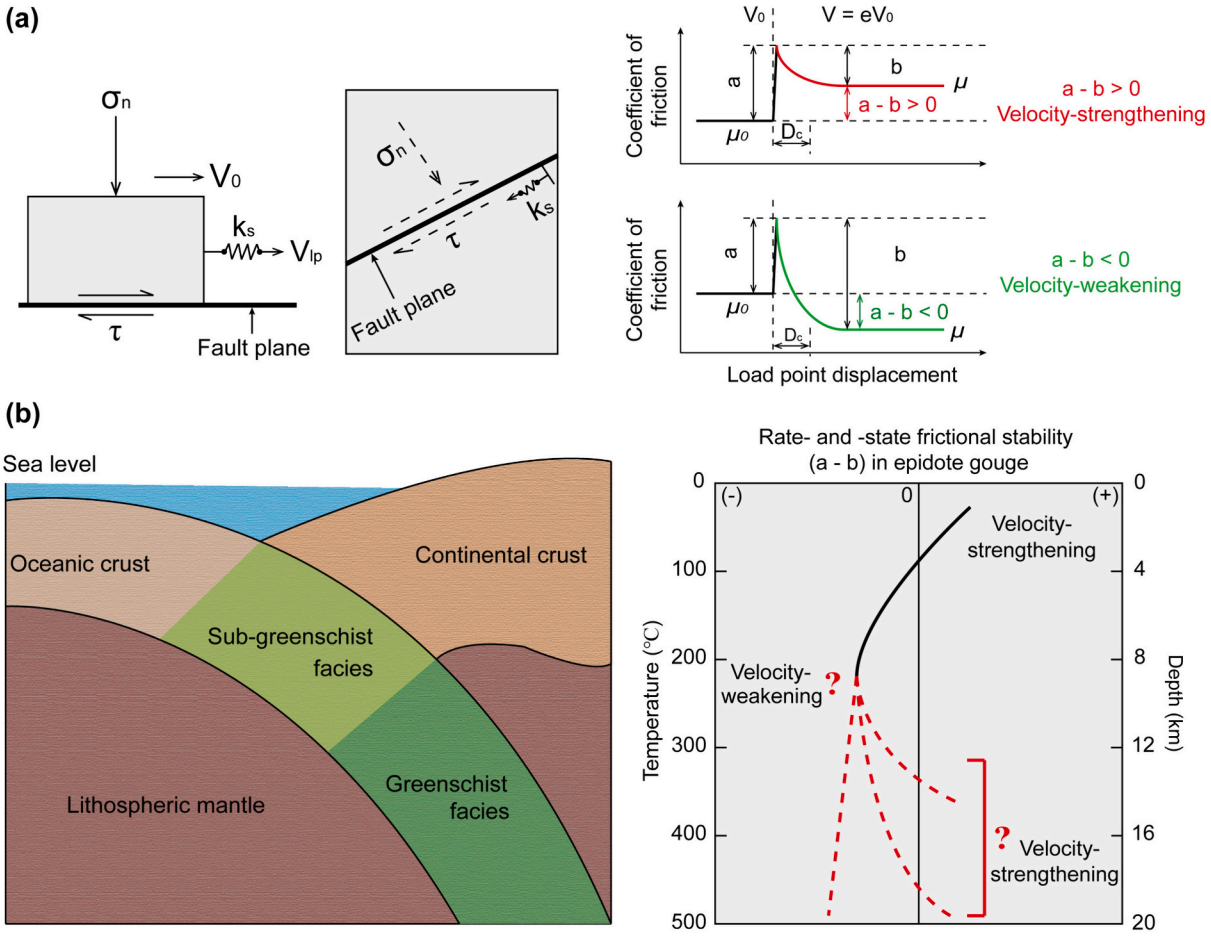

Fig. 1. (a) Conceptual sliding model for fault sliding behavior, and the idealized rate-and-state friction response at a velocity up-step: velocity-strengthening (*v-s*) and velocity-weakening (*v-w*). Symbols k_s and V_{lp} represent the system (spring) stiffness and load point velocity, respectively. (b) Schematic of greenschist metamorphism within a subducting slab and the corresponding rate-and-state frictional stability ($a - b$) in epidote gouge. The temperature/depth on (b)-right corresponds to the cartoon in (b)-left by considering a thermal gradient of 25 °*C/km*.

$$\frac{d\theta}{dt} = -\frac{V\theta}{D_c} ln\left(\frac{V\theta}{D_c}\right) \text{ (slip law)} \quad (4)$$

where μ_0 and μ represent the steady state coefficient of friction at the reference shear velocity V_0 and the instantaneous coefficient of friction at the current shear velocity V. a and b are two dimensionless parameters that describe the direct and evolutional effects from the velocity step, respectively, D_c is the required critical slip distance from a past to a new steady state and θ describes the contact age and could be described from either the slowness or slip law in Eqs. (3)–(4). An idealized rate-and-state friction response for a velocity up-step is shown in Fig. 1a.

At steady state, the state variable θ is constant and the frictional stability $(a - b)$ can be generated from Eqs.(2)–(4), as,

$$a - b = \frac{\Delta\mu_{ss}}{\Delta ln V} \quad (5)$$

where $\Delta\mu_{ss}$ denotes the difference in coefficients of friction before and after the velocity change. Positive values of $(a - b)$ indicate an enhanced frictional strength from a velocity up-step, representing velocity-strengthening behavior. Faults with positive values of $(a - b)$ favor only stable and aseismic sliding. Conversely, negative values of $(a - b)$ denote velocity-weakening behavior and promote unstable and seismic fault sliding whenever the fault stiffness is lower than the rheologic critical stiffness of the loading medium (Gu et al., 1984). The impacts of geological (including mineralogy and fault roughness) and environmental (including the temperature and applied pressure) conditions on fault response are reflected in the frictional constitutive parameters a, b and D_c (den Hartog and Spiers, 2013; Fang et al., 2018). Additionally, changes in the values of a, b and D_c also depend on microstructural evolution. Thus, the rate-and-state frictional response, especially frictional stability $(a - b)$ is vital in understanding mechanisms controlling the evolution of fault stability and geodynamic process under hydrothermal conditions.

To explore the controls of epidote on faulting styles in greenschist facies we complete laboratory velocity-stepping experiments on pure epidote gouge at temperatures up to 500 °C and effective stresses up to 300 MPa to (1) define the temperature dependence of rate-and-state friction parameters in epidote gouge, as represented in Fig. 1b, (2) examine the effect of fluid pressurization on the stability response of epidote gouge at high temperatures, and (3) explore related implications for a stability-instability-stability transition in faults subducting under greenschist facies conditions.

2. Experimental methods

We complete a series of frictional sliding experiments under greenschist facies conditions on powdered epidote gouges under independently controlled temperatures and effective stresses modulated by fluid overpressures. We use the experimental observations to define anticipated changes in styles in faulting with depth and time.

2.1. Epidote gouge preparation

The epidote (Fig. 2a) used in the shear experiments was recovered

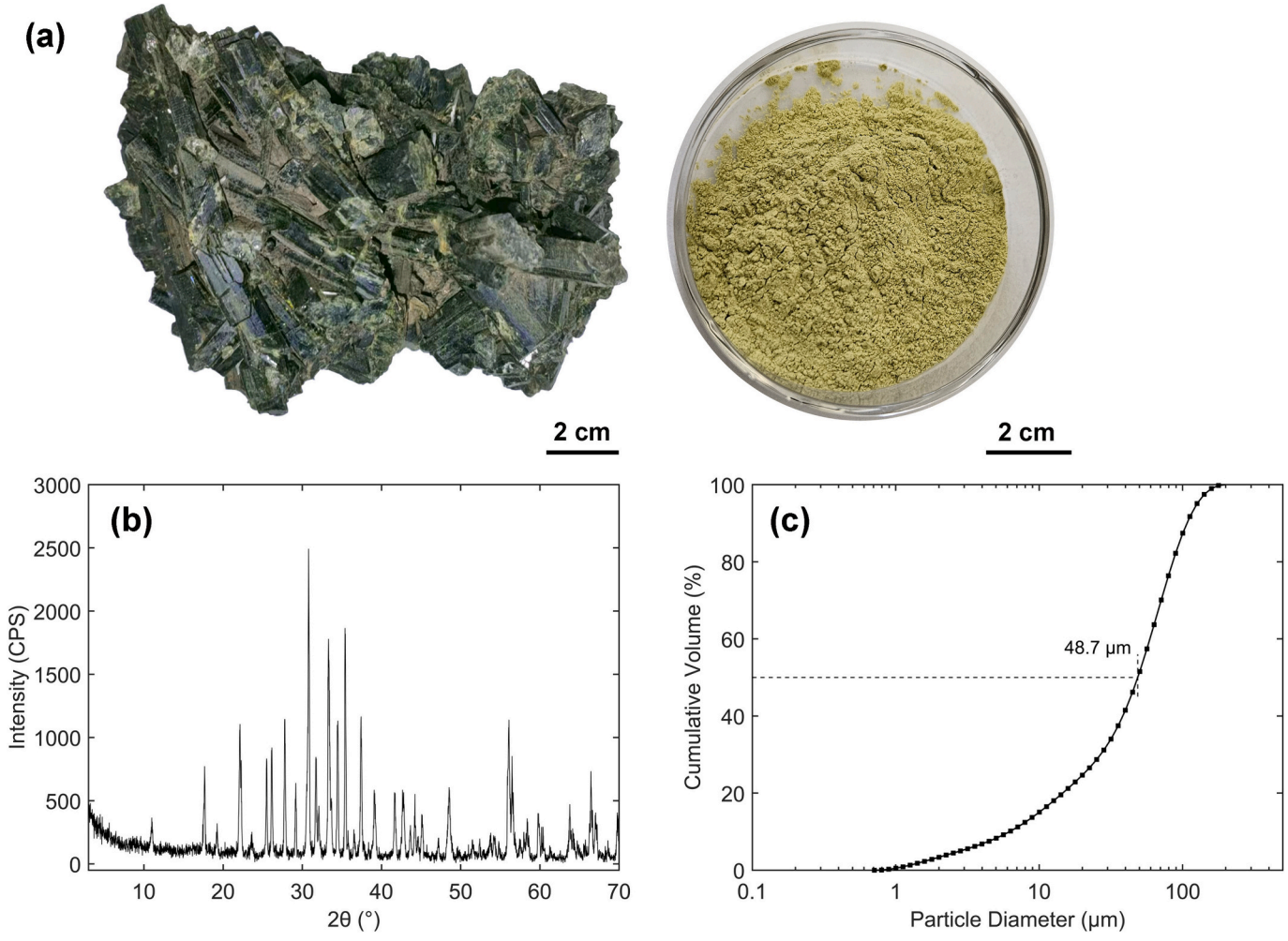

Fig. 2. (a) Powdered epidote with corresponding (b) X-ray diffraction (XRD) results and (c) particle size distribution.

from Handan city, Hebei Province, northern China. Surface impurities were removed and the epidote powdered to particles <75 μm to represent fault gouge (Fig. 2a). The mineral composition was determined with the X-ray diffraction method, which showed an epidote powder of >99 % purity (Fig. 2b). Laser classifier (Fig. 2c) defined diameters of ~90 % epidote particles to be <75 μ*m*, with a median particle diameter of ~48.7 μ*m*.

2.2. Experimental apparatus and procedures

Velocity-stepping shear experiments were completed using the gas-confined triaxial shear assembly shown in Fig. 3 - with a detailed description presented in He et al. (2006). For each test, the upper and lower cylindrical forcing blocks were prepared from gabbro – with a diameter of 19.8 *mm* and a height of 40 *mm* and with an inclined saw cut at 35° to the cylinder axis to accommodate shear of the confined gouge layer. The gabbro driving blocks were first ground flat, and then roughened by 300-mesh silicon carbide (SiC) abrasive to drive the gouge layer in shear. The upper driving block was drilled with two interconnected holes (shown in Fig. 3) for the pore fluid entry. Dense brass filters with micrometer-sized pores (pore diameters on the order of micrometers) were inserted into these two holes to prevent gouge extrusion and ensure the supply of pore fluids and pressures. The epidote powder was prepared as a paste using deionized (DI) water and placed on the upper driving block, before mating with the lower driving blocks. Under high-temperature and high-pressure conditions, the DI water is highly reactive with the gouge and forcing blocks and would be expected to influence pressure-solution processes on lab timescales. During our shear experiments, we typically leave 2–3 h to ensure that the pore fluid is uniformly distributed within the gouge zone and this period of time may allow the gouge sample or forcing blocks to chemically equilibrate with the DI water and minimize any transient chemical effects. The thickness of the epidote gouge was precisely controlled to be 1.0 *mm* by a high-precision leveling jig. Subsequently, the gouge-filled driving blocks were inserted into a 0.35-*mm* thick annealed copper jacket, with cylindrical tungsten carbide and corundum blocks arranged above and below the sample as forcing platens. The space between the copper jacket and furnace was filled with boron nitride powders to inhibit convection of the argon gas confining fluid. The O-rings on both steel end plugs seals the fault gouge zone, while the high-pressure seal at the top sealing block and upper piston maintains the sealing of the entire system. Finally, a thermocouple was inserted in the upper forcing block to record the gouge midpoint temperature at a distance of ~8.72 *mm* from the thermocouple to gouge midpoint. Uniform temperature along the sample was maintained by a two-zone internal furnace returning a near-zero vertical gradient.

A total of eight shear experiments were completed at temperatures (T) of 100–500 °*C*, confining pressures (σ_c) of 125–170 *MPa* and pore fluid pressures (P_f) of 30–75 *MPa*, with experimental details given in Table 1. The eight experiments can be divided into two distinct groups according to their respective objectives. The five experiments in group I, including Ep-100, Ep-200, Ep-300, Ep-400 and Ep-500, were completed at constant confining (σ_c = 125 *MPa*) and pore fluid (P_f = 30 *MPa*) pressures but at different temperatures. These were to explore the effect of temperature evolution with depth on epidote gouge friction and stability. The final three experiments, including Ep300–125-75,

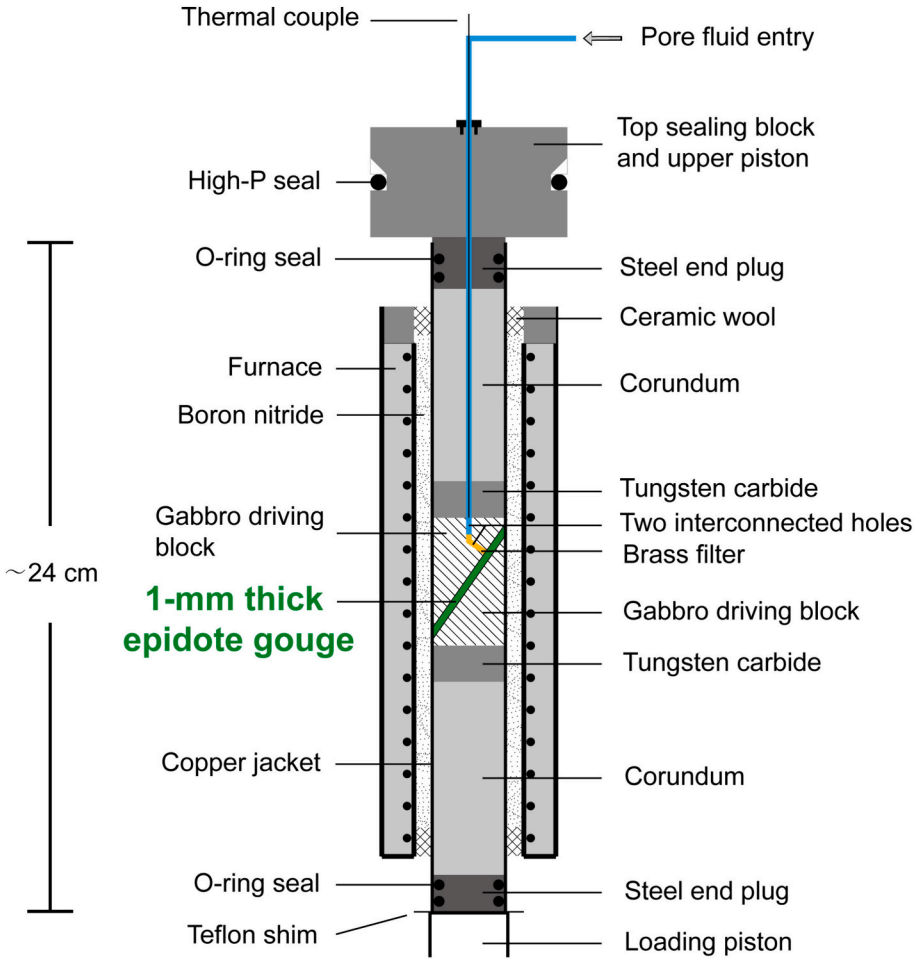

Fig. 3. Schematic of fault gouge assembly in the triaxial shear apparatus.

Table 1
Suite of experimental conditions. Symbols and abbreviations T, σ_c, P_f, σ_{ceff}, σ_{neff}, D_t, *v-s*, and *v-w* represent applied temperature, confining pressure, pore fluid pressure, effective confining pressure, and effective normal stress, together with observed total shear displacement and designation as to whether velocity-strengthening, or velocity-weakening behaviors, are observed, respectively. The confining and pore fluid pressures are kept constant during the experiments, while the effective normal stress would change slightly with the velocity steps. Thus, the listed values of effective normal stress are approximate values.

Experiment number	T (°C)	σ_c (MPa)	P_f (MPa)	σ_{ceff} (MPa)	σ_{neff} (MPa)	Axial velocities (μm)	D_t (mm)	Velocity dependence	Occurrence of stick-slips or oscillations
Group I: Constant pressure condition ($\sigma_c = 125$ MPa and $P_f = 30$ MPa)									
Ep-100	100	125	30	95	~200	1–0.2–0.04–0.2-1-0.2–0.04–0.2	3.86	*v-s*, *v-w*	–
Ep-200	200	125	30	95	~200	1–0.2–0.04–0.2-1-0.2–0.04	3.73	*v-w*	All velocity steps
Ep-300	300	125	30	95	~200	1–0.2–0.04–0.2-1-0.2–0.04–0.2	3.76	*v-w*	All velocity steps, except for second 0.04 μm/*s*
Ep-400	400	125	30	95	~200	1–0.2–0.04–0.2-1-0.2–0.04–0.2	3.70	*v-s*	–
Ep-500	500	125	30	95	~200	1–0.2–0.04–0.2-1-0.2–0.04–0.2	3.70	*v-s*	–
Group II: Constant temperature condition ($T = 300$ °C)									
Ep300–125-75	300	125	75	50	~100	1–0.2–0.04–0.2-1-0.2–0.04–0.2-1	3.87	*v-w*	All velocity steps
Ep300–170-30	300	170	30	140	~300	1–0.2–0.04–0.2-1-0.2–0.04–0.2	3.94	*v-s*, *v-w*	First and second 0.2 μm/*s*, second 1 μm/*s*
Ep300–170-75	300	170	75	95	~200	1–0.2–0.04–0.2-1-0.2–0.04–0.2-1	3.86	*v-s*, *v-w*	First and second 0.2 $\mu m/s$, second and third 1 $\mu m/s$

Ep300–170-30, and Ep300–170-75, were performed at constant temperature ($T = 300$ °C) but different fluid pressures, to investigate the impact of different fluid pressure to normal stress ratios on epidote gouge stability.

As the gas and fluid pressures in the triaxial sample assembly would increase as temperatures were elevated, the confining and pore fluid pressures were first raised to approximately one third of the desired end-values, followed by heating and adjusting the confining and pore fluid pressures to the desired values. Deionized water was adopted as the pore fluid to minimize unwanted chemical effects. The axial load, displacement and temperature were recorded by the high-resolution internal load sensor (with resolution of ±0.1 N), external displacement sensor (with resolution of ±0.1 μm and range of 0–10 mm), and an external thermocouple (with resolution of ±1 °C and range of 0–1000 °C), respectively, at a sampling frequency of 1 Hz. The epidote gouge was initially sheared at an axial velocity of 1 μm/s until the slip-strengthening trend is gentle, followed by up- then down-stepping the axial velocities between 1 and 0.2–0.04–0.2-1 $\mu m/s$ (corresponding to velocities of 1.22–0.244-0.0488-0.244-1.22 μm/s along the shear direction) to assess the velocity dependence of friction evolution. The total duration of the shear experiment is ~11 h and the time taken to allow saturation of the gouge layer is 2–3 h under both high-temperature and high-pressure conditions before shearing initiated.

2.3. Data reduction and pretreatment

Variation in the epidote gouge contact area with increasing displacement and the changing shear resistance from the copper jacket required correction of the raw data, with detailed descriptions of these corrections reported in He et al. (2006). The coefficient of friction (μ) is recovered from Eq. (1) by assuming zero cohesion. Fault frictional stability ($a - b$) is calculated from rate-and-state friction (RSF) following Eqs. (2)–(5) with velocity-strengthening or velocity-weakening represented by ($a - b$) values as shown in Fig. 1a. For fault response with stick-slip, the values of ($a - b$) were calculated from the average values of stress drops. It should be noted that these ($a - b$) values obtained from the stick-slips are only approximate as the obtained values depend on the critical slip distance D_c, which could vary within the experiments.

After the shear experiments, the deformed gouges were first dried in a drying oven at a temperature of 65 °C for ~48 h and then vacuum impregnated with epoxy resin. Subsequently, the samples were thin sectioned along the shear directions and perpendicular to strike following the standard thickness, then polished and gold-coated for imaging by scanning electron microscopy (SEM). Additionally, as the tested gouge in each shear experiment is generally less than 1.5 g and the epidote minerals generally contain ~2 wt% bound water in their crystal structures, the alteration products would be very limited (<0.03 g). Consequently, we did not conduct post experimental geochemical analyses.

3. Results – friction/stability behavior

3.1. Friction/stability at elevated temperatures

By performing experiments at a constant pressure but different temperatures, we can isolate the effect of temperature on the evolution of friction and frictional stability of the epidote gouge. A quasi-linear increase in friction is apparent within the initial 1.0 mm displacement followed by macroscopic yield and slight displacement-strengthening response over the remaining displacement (Figs. 4 and S2). At temperatures of 100, 400 and 500 °C (Fig. 4a and d-e), the epidote gouge exhibits only stable sliding. However, at temperatures of 200–300 °C (Figs. 4b-4c), stick-slip initiates at almost all velocities, indicative of the potential for seismic response (Brace and Byerlee, 1966). The magnitudes of the individual stress drops also increase with elevated temperature with the maximum friction drops reaching ~0.03 at 200 °C and ~ 0.052 at 300 °C, respectively, occurring at the lowest velocity.

The coefficients of friction (μ) across the tested temperature range (100–500 °C) approach ~0.73 and are insensitive to temperature (Fig. 5 and Table 2). This frictional strength is high compared to other hydrous mineral gouges, such as chlorite ($\mu = 0.2$–0.4) (Okamoto et al., 2019), talc ($\mu < 0.3$) (Moore and Lockner, 2008), and lizardite serpentinite ($\mu =$ 0.15–0.35) gouges, but similar to amphibolite (0.67–0.73) (Liu and He, 2020) and antigorite serpentinite ($\mu = 0.50$–0.85) (Reinen et al., 1994) gouges. Conversely, elevated temperatures exert a significant control on frictional stability. As the temperature increases, the epidote gouge transitions from velocity-neutral behavior at 100 °C ($a - b = -0.0005$ to 0.0018), to velocity-weakening behavior at 200 °C ($a - b = -0.0187$ to -0.0076) and 300 °C ($a - b = -0.0339$ to -0.0185), then back to velocity-strengthening behavior at 400 °C ($a - b = 0.0040$ to 0.0094) and 500 °C ($a - b = 0.0052$ to 0.0092) (Fig. 6 and Table 2) - indicating the destabilizing effects of temperature in the range $100 < T < 300$ °C. This first stability transition is similar to results for epidote vein gouge (stability to instability occurring at 105 °C) under hydrothermal conditions as reported by Kolawole et al. (2019) although they used the average friction values to obtain ($a - b$) for stick-slips. In addition, we

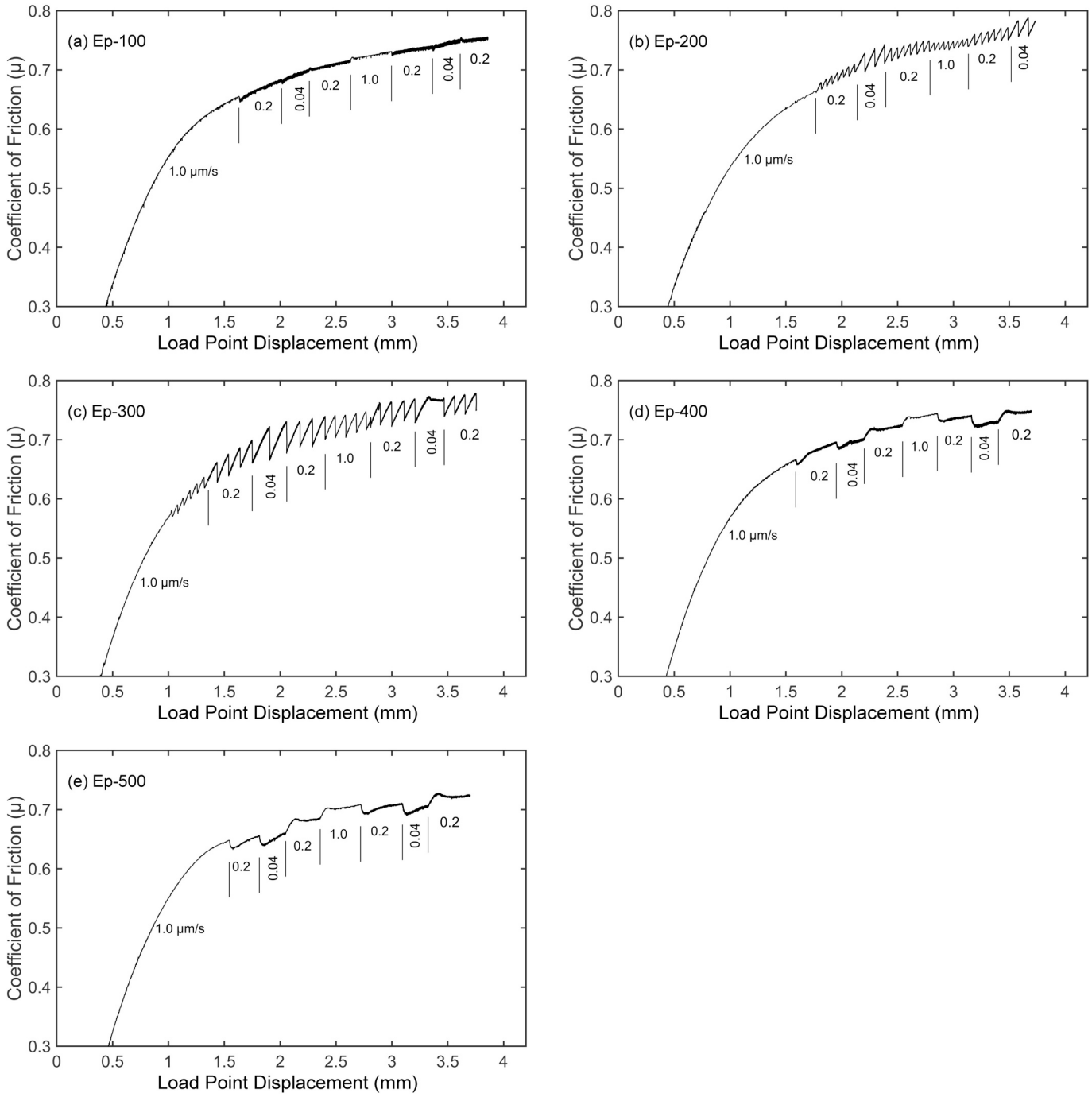

Fig. 4. Coefficient of friction (μ) versus shear displacement for tests at the uniform confining pressure (125 *MPa*) and pore fluid pressure (30 *MPa*) but different temperatures (100–500 °*C*). Experiment numbers: (a) Ep-100, (b) Ep-200, (c) Ep-300, (d) Ep-400, and (e) Ep-500. Incremented/decremented shearing velocities are marked below the curves.

also examined the velocity dependence of ($a - b$) values at $T = 100$–500 °C in Fig. 7. Values of ($a - b$) at $T = 100$ and 400–500 °C are less affected by the upward or downward velocity steps. However, the values of ($a - b$) at $T = 200$–300 °C are apparently affected by the upward or downward variation of velocities. Besides, the magnitudes of our obtained positive ($a - b$) values are small compared to values reported in other friction experiments under hydrothermal conditions (e.g., Blanpied et al., 1995; Niemeijer et al., 2016; Verberne et al., 2015), but similar with the results from Tian and He (2019) and Liu and He (2020). This discrepancy may derive from different testing conditions and shear apparatus.

3.2. Friction/Stability at elevated fluid pressures

To explore the effect of elevated fluid pressure within the slab, driven by dehydration reactions, the pore fluid pressures were increased at both low ($\sigma_c = 125$ *MPa*) and high ($\sigma_c = 170$ *MPa*) confining pressures, with the friction-displacement and friction-effective normal stress curves shown in Figs. S3 and S4, respectively. At a low confining pressure ($\sigma_c =$ 125 *MPa*), elevating the pore fluid pressures to 75 *MPa* in test Ep300–125-75 returns larger stick-slips for each velocity than for test Ep-300 (Figs. 4c and S3a) – an indicator of enhanced frictional instability. At a high confining pressure ($\sigma_c = 170$ *MPa*), elevating the pore

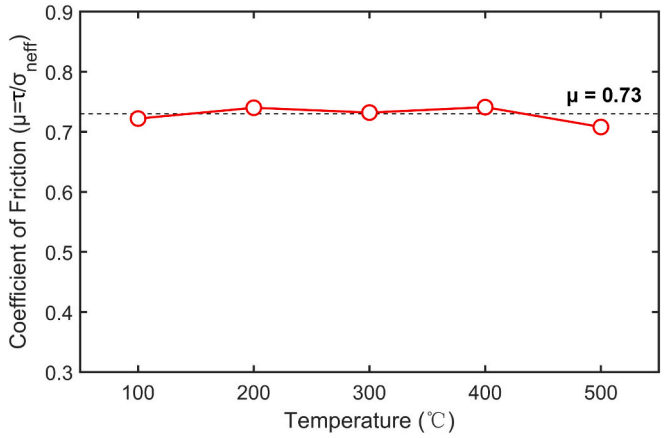

Fig. 5. Evolution of frictional strength with temperature (μ) for epidote gouge at $\sigma_c = 125$ *MPa* and $P_f = 30$ *MPa*. Black dashed line defines mean friction as $\mu = 0.73$.

fluid pressure also promotes larger stick-slips (Figs. S3b-S3c), similar with the trend at a low confining pressure. Additionally, compared with the experiments at low confining pressure, the high confining pressure at tests Ep300–170-30 and Ep300–170-75 also enhances stable sliding and velocity-strengthening response (Figs. S3b-S3c).

At a low confining pressure ($\sigma_c = 125$ *MPa*) (Figs. 8a-8b and Table 2), elevating the pore fluid pressure would slightly increase the epidote gouge coefficients of friction from 0.732 to 0.779 and apparently lower the ($a - b$) values from within the range of −0.0339 to −0.0185 to the range of −0.0373 to −0.0277. The variation in coefficient of friction at a high confining pressure ($\sigma_c = 170$ *MPa*) (Figs. 8c and Table 2) is similar to that at low confining pressure. However, only the ($a - b$) values at velocities exhibiting stick-slip behaviors apparently decrease with an increase in pore fluid pressure (Fig. 8d and Table 2). By examining the effect of decreased effective normal stress in Figs. 9a-9b, it is apparent that, with a decrease in effective normal stress, the coefficients of friction increase slightly from 0.73 to 0.74 at $\sigma_{neff} = 200$ and 300 *MPa* to ~0.78 at $\sigma_{neff} = 100$ *MPa* (Fig. 9a and Table 2). Meanwhile, frictional instability is enhanced at higher effective normal stresses (Fig. 9b), with values of ($a - b$) decreasing from −0.0198 to 0.0017 at $\sigma_{neff} = 300$ *MPa*, to −0.0339 to −0.0185 at $\sigma_{neff} = 200$ *MPa*, and to −0.0373 to −0.0277 at $\sigma_{neff} = 100$ *MPa* (Table 2). In addition, decreasing the confining pressure also has only a negligible effect on coefficient of friction (Fig. 9c) but apparently further promotes fault instability (Fig. 9d). These results all show that either elevating the pore fluid pressure or decreasing the effective stress, each promote unstable sliding. However, we note that changes in pore pressure are not intrinsically isolated from effective normal stress in our test suite. The discussions on the effect of pore fluid pressure in Fig. 8 are not based on the constant effective normal stress, while the discussions on the effect of effective normal stress in Fig. 9 are also not based on the constant pore fluid pressure.

3.3. Microstructural development

Following the methods described in Section 2.3, the microstructures of deformed epidote gouges were obtained from scanning electron microscopy (SEM) with the shear fabrics described following the terminology of Logan et al. (1992) (Fig. S5). The most common features of deformed fault gouge fabrics are R_1 and Y shears with both indicating localized shear zones. The R_1 fractures typically show a low angle (<30°) to the interface parallel with the forcing block, while the Y fractures are nearly parallel with the forcing block interface (Logan et al., 1992).

Backscattered microscopic images at different temperatures (T = 100–500 °C) are shown in Figs. 10–11 with the microstructures of epidote gouges returning velocity-strengthening response quite different from those returning velocity-weakening or stick-slip responses. At T = 100 °C, the epidote gouge returns velocity-neutral behavior and the deformed gouge shows apparent particle extrusion and crushing (Figs. 10a and 11a). Apparent R_1 shear fabrics could also be observed with particle diameters at the R_1 shear zone <10 μm due to the effect of strong shear (Fig. 11b). The areas outside the R_1 shear zone show apparent particle granular flow, with particles undergoing weaker shear (Fig. 10a). At $T = 200$ °C, the epidote gouge returns velocity-weakening behavior and minor stick-slips and the R_1 shears are closer together (Fig. 10b). When the temperature increases to $T = 300$ °C, the epidote gouge shows apparent stick-slip behavior and Y shears are observed throughout the shear zone (Fig. 10c). The Y shears generally appear with the fault sliding potentially changing from stable slip to apparent stick-slips according to Logan et al. (1992), consistent with the stick-slip

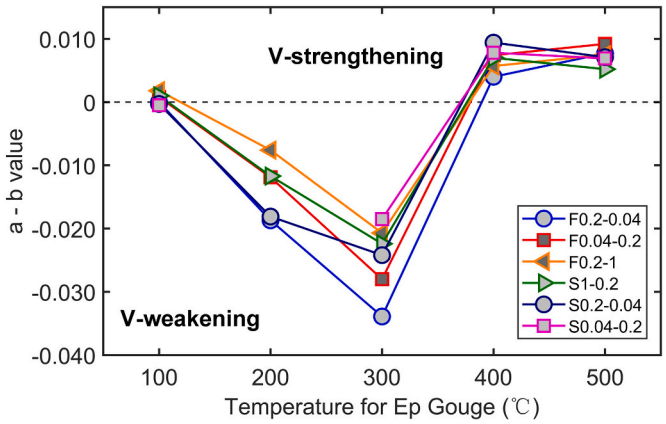

Fig. 6. Frictional stability ($a - b$) for epidote (Ep) gouge at $\sigma_c = 125$ *MPa*, $P_f = 30$ *MPa* and temperatures (100–500 °C). Legend shows the sequence of velocity steps, with "F" and "S" representing first and second, respectively.

Table 2
Experimental results for coefficient of friction (μ_{ss}) and frictional stability ($a - b$). The coefficients of friction (μ_{ss}) were evaluated at a shear displacement of ~2.75 *mm* and a shear velocity of 1.22 μm/*s*. Symbols for 'F(irst)' and 'S(econd)' indicate the sequence of shear velocity steps.

Experiment number	μ_{ss}	Values of ($a - b$) at different axial velocities (μm/*s*)						
		F0.2–0.04	F0.04–0.2	F0.2–1.0	S1.0–0.2	S0.2–0.04	S0.04–0.2	S0.2–1.0
Ep-100	0.722	0	0.0008	0.0018	0.0010	−0.0003	−0.0005	–
Ep-200	0.740	−0.0187	−0.0119	−0.0076	−0.0117	−0.0181	–	–
Ep-300	0.732	−0.0339	−0.0280	−0.0207	−0.0224	−0.0242	−0.0185	–
Ep-400	0.741	0.0040	0.0074	0.0057	0.0070	0.0094	0.0078	–
Ep-500	0.708	0.0077	0.0092	0.0075	0.0052	0.0071	0.0069	–
Ep300–125-75	0.779	−0.0373	−0.0363	−0.0282	−0.0322	−0.0326	−0.0299	−0.0277
Ep300–170-30	0.735	−0.0198	−0.0141	−0.0112	−0.0105	0.0020	0.0017	–
Ep-300-170-75	0.754	−0.0277	−0.0220	−0.0209	−0.0168	−0.0013	0.0037	−0.0121

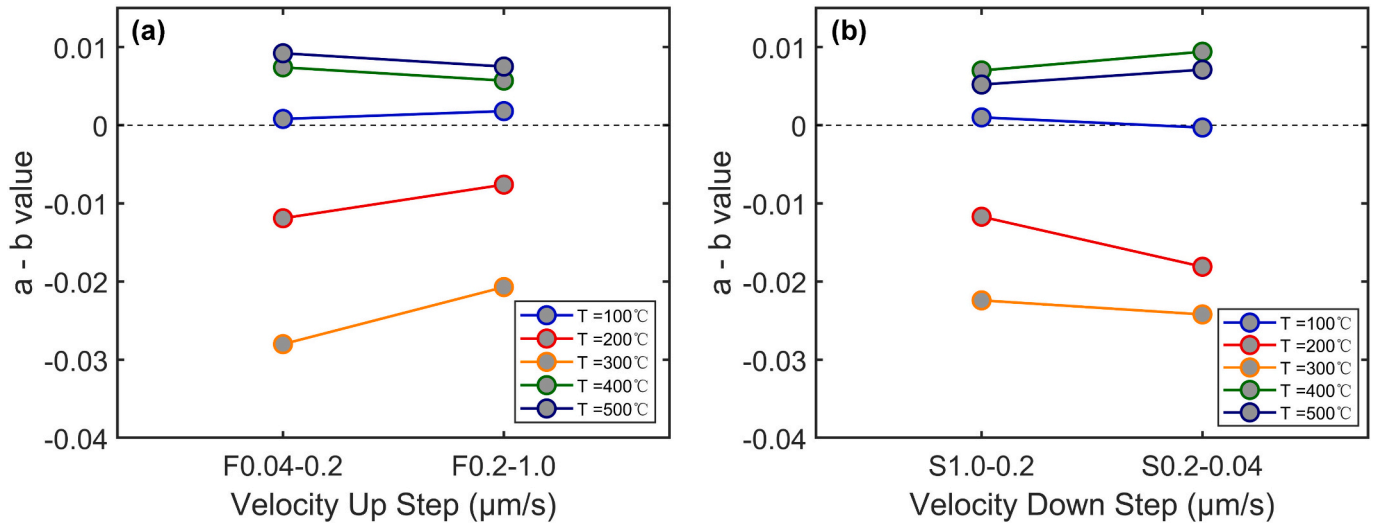

Fig. 7. Frictional stability ($a - b$) for epidote (Ep) gouge at $\sigma_c = 125$ *MPa*, $P_f = 30$ *MPa*, $T = 100$–500 °*C* and different shear velocities, (a) velocity up steps and (b) velocity down steps. Legend shows the testing temperature.

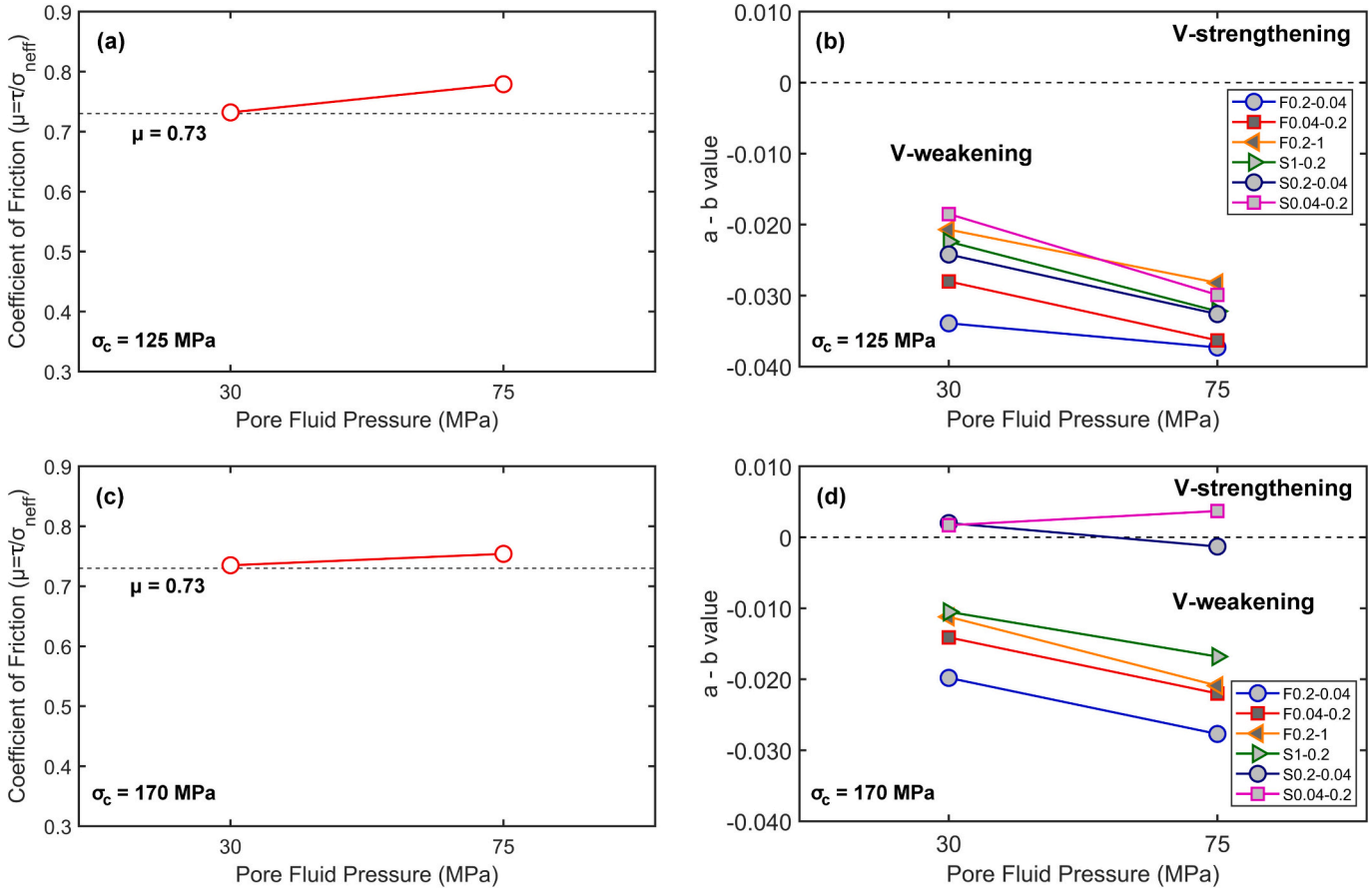

Fig. 8. (a) Coefficient of friction (μ) and (b) frictional stability ($a - b$) at $T = 300$ °*C*, $\sigma_c = 125$ *MPa* and $P_f = 30$ & 75 *MPa*. The comparisons in (a) and (b) are based on tests Ep300 and Ep-300-125-75. (c) Coefficient of friction (μ) and (d) frictional stability ($a - b$) at $T = 300$ °*C*, $\sigma_c = 170$ *MPa* and $P_f = 30$ & 75 *MPa*. The comparisons in (c) and (d) derive from tests Ep300–170-30 and Ep300–170-75.

response in experiment Ep-300. In addition, the Y shear zones also undergo strong particle crushing with diameters of most particles <5 μ*m* (Fig. 11d). However, at $T = 400$ and 500 °*C*, the epidote gouges return velocity-strengthening responses and also show apparent R_1 shear zones but no visible fractures - possibly as these zones are more highly compacted and do not dilate upon decompression. Meanwhile, the deformed gouges show only a minor amount of grain size reduction at $T = 400$–500 °*C* (Figs. 10d-e, 11e-f). Backscattered microscopic images at $T = 300$ °*C* but different pressures are shown in Fig. 12 where R_1 shears dominate the shear fabrics. Upon elevated pore pressure in Experiment Ep300–125-75, dilatant granular flow with a higher porosity (more apparent void) is observed with grain sizes less reduced as a result of

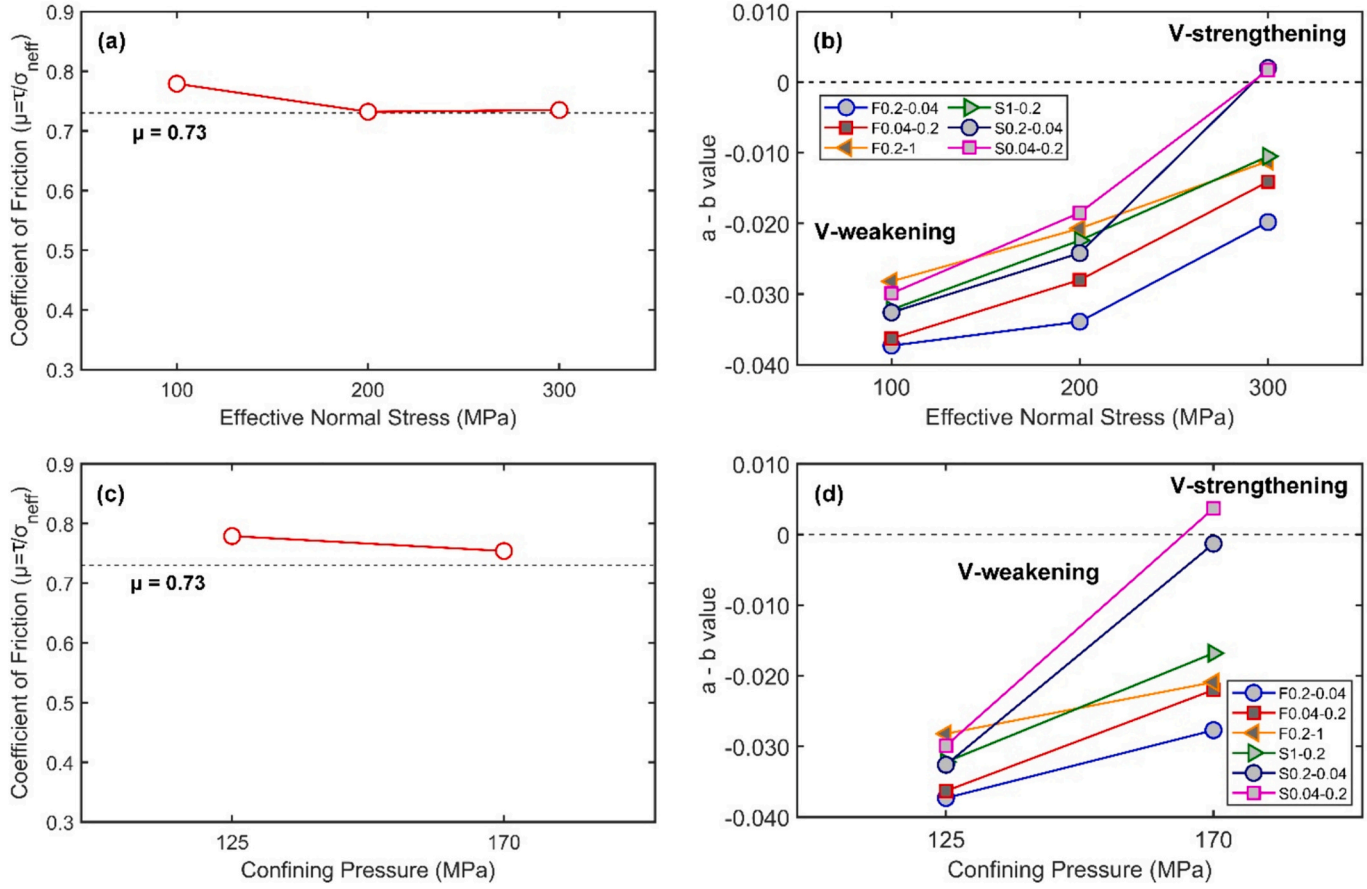

Fig. 9. (a) Coefficient of friction (μ) and (b) frictional stability ($a-b$) at constant temperature ($T = 300\ ^{\circ}C$) but varying effective normal stresses. The comparisons in (a) and (b) are based on tests Ep300–125-75, Ep300, and Ep300–170-30. (c) Coefficient of friction (μ) and (d) frictional stability ($a-b$) at constant temperature ($T = 300\ ^{\circ}C$) and pore fluid pressure ($P_f = 75\ MPa$) but varying confining pressures. The comparisons in (c) and (d) are based on tests Ep300–125-75 and Ep300–170-75.

shear comminution (Fig. 12a and d-e).

4. Discussion

4.1. Comparison with previous observations

Frictional stability ($a-b$) in the epidote gouge at a constant effective stress ($\sigma_{neff} = 200\ MPa$ and $P_f = 30\ MPa$) is sensitive to increasing temperature, i.e., velocity-neutral at $T = 100\ ^{\circ}C$, velocity-weakening with stick-slips at $T = 200$–$300\ ^{\circ}C$, then again velocity-strengthening at $T = 400$–$500\ ^{\circ}C$ (Fig. 7). The first transition from velocity-strengthening to velocity-weakening at a temperature of $\sim 100\ ^{\circ}C$ is significantly lower than for gouges comprising most common hydrous minerals – including sheet-structured chlorite and talc, hornblende and glaucophane-lawsonite (Liu and He, 2020; Moore and Lockner, 2008; Okamoto et al., 2019; Sawai et al., 2016). Chlorite gouge only exhibits minor velocity-weakening behavior at $T = 300\ ^{\circ}C$ at total normal stresses of 100–400 *MPa* and pore fluid pressures of 50–220 *MPa* across a testing temperature range of 22–600 $^{\circ}C$ (Okamoto et al., 2019). Similarly, the talc gouge shows only velocity-strengthening and inherently stable behavior over the temperature range 25–400 $^{\circ}C$ (Moore and Lockner, 2008). Chlorite and talc are both phyllosilicate minerals and their layered crystal structure and weak interlayer bonds typically contribute to low frictional strength and velocity-strengthening behavior (Giorgetti et al., 2015; Ikari et al., 2009; Moore and Lockner, 2008, 2011). Additionally, simulated hornblende gouges show velocity-strengthening response at $T = 100$–$200\ ^{\circ}C$ and minor velocity-weakening response at $T = 300$–$600\ ^{\circ}C$ at a confining pressure of 136 *MPa* and a pore fluid pressure of 30 *MPa* (Liu and He, 2020). Similarly, glaucophane-lawsonite mixed gouges only exhibit velocity-weakening behavior at $T = 200$ and $400\ ^{\circ}C$ at effective normal stresses in the range 25–200 *MPa* and pore fluid pressures of 25–200 *MPa* (Sawai et al., 2016). These comparisons demonstrate that an abundance of epidote gouge within subduction zone faults could allow the nucleation of earthquakes at a lower temperature than most of the common hydrous minerals. Meanwhile, the occurrence of epidote is closely related to retrograde metamorphism of plagioclase and augite, with calcium family minerals (like calcite) also contributing to the abundance of epidote under greenschist metamorphic conditions (Franz and Liebscher, 2004; Spinelli and Wang, 2009). The first transition temperature from velocity-strengthening to velocity-weakening at $\sim 100\ ^{\circ}C$ is similar to gouges rich in plagioclase ($\sim 100\ ^{\circ}C$) (He et al., 2013), augite ($\sim 100\ ^{\circ}C$) (Tian and He, 2019) and calcite (even $<100\ ^{\circ}C$) (Verberne et al., 2015).

In addition to temperature, effective normal stresses or pore fluid pressures also affect the stability of subduction zone faults (den Hartog et al., 2012; den Hartog and Spiers, 2013). At $T = 300\ ^{\circ}C$, a decrease in effective normal stress or an increase in pore fluid pressure both destabilize the epidote gouge (Figs. 8–9). This indicates that epidote gouge stability is also sensitive to the variation in effective normal stress or pore fluid pressure. This observation that decreasing the effective normal stress destabilizes the fault is opposite to results on quart-clay mixed gouge (den Hartog and Spiers, 2013), but congruent with several experimental studies, including those on phyllosilicate-bearing gouges (Niemeijer and Collettini, 2014), glaucophane-lawsonite mixed gouges (Sawai et al., 2016) and granitic gouges (Zhang et al., 2022). This discrepancy may result from either the different testing materials or conditions. More importantly, a lower effective stress would tend to

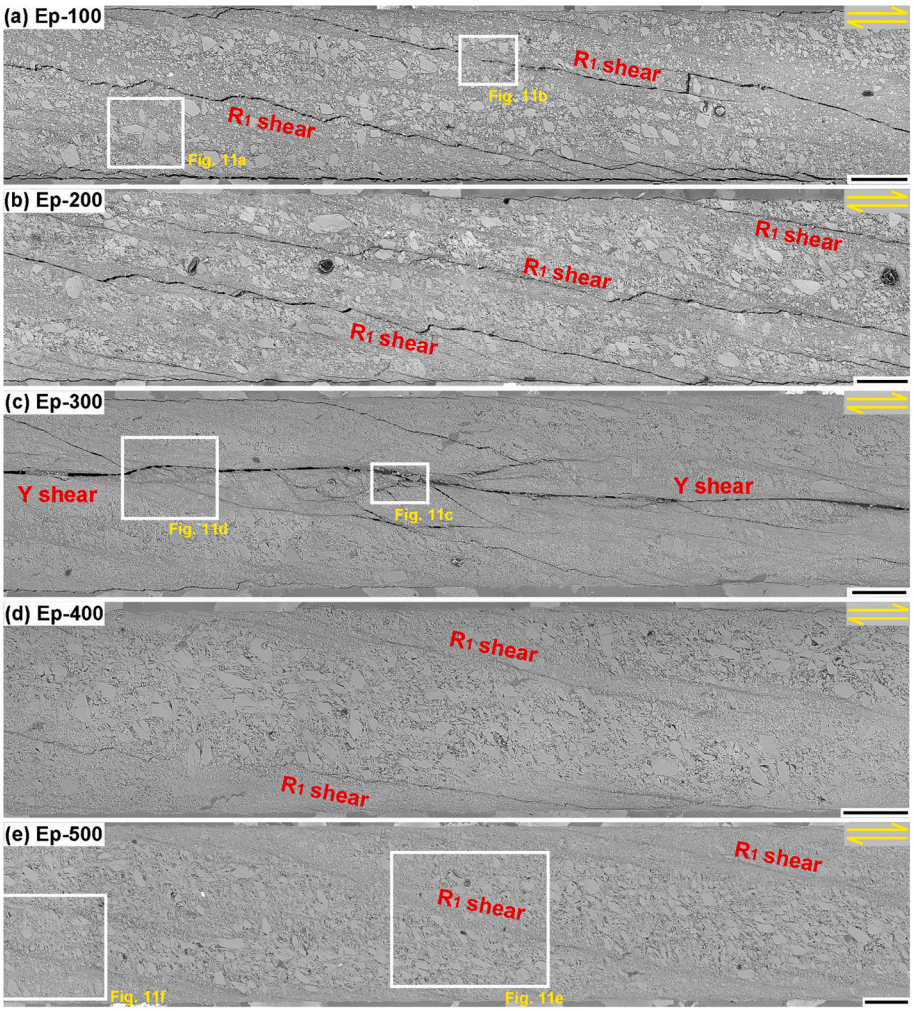

Fig. 10. Backscattered microstructural images of the deformed gouges at $\sigma_c = 125$ *MPa*, $P_f = 30$ *MPa* and different temperatures ($T = 100$–500 °*C*), (a) Ep-100, (b) Ep-200, (c) Ep-300, (d) Ep-400, and (d) Ep-500. Scale bars, 200 μ*m*. The zoom-in pictures of the white rectangles are shown in Fig. 11.

stabilize slip, but if the lower effective stress also changes the stiffness (of the apparatus and fault surroundings), it could potentially lead to more unstable slip (Im et al., 2017). Also, lowering the effective stress could affect gouge particle compaction and the particle size and thus change values of D_c. Meanwhile, the lower effective stress could enhance fault embrittlement and localized shear. This could further lower the contact area for the gouge particles and increase b values. These changes all could affect fault critical stiffness and hence fault instability.

4.2. Mechanisms of epidote instability at different temperatures and pressures

Observed variations of frictional stability ($a - b$) of epidote gouge at different temperatures and pressures can be partially understood by a microphysical model proposed by Niemeijer and Spiers (2007). Although this model was initially proposed to explain the strong velocity weakening behavior in phyllosilicate-bearing gouges, it has broad applications to understand the velocity-strengthening to weakening transition with increasing temperatures or pressures (Boulton et al., 2014; den Hartog and Spiers, 2014; Sawai et al., 2016). In the microphysical model, fault instability is modulated by granular flow-induced gouge dilation and the competition with pressure solution-induced compaction. Pressure solution involves water-mediated mineral particle dissolution, transport and precipitation. Although we do not find the direct evidence of pressure solution in the microstructural observations, epidote exhibits comparable solubility and dissolution rates to feldspars (like the K-feldspar and albite) and micas at low temperatures (Rose, 1991; Kalinowski et al., 1998; Poli and Schmidt, 2004; Marieni et al., 2021). This further supports the applicability of the microphysical model.

At low temperatures (e.g., $T < 100$ °*C* for epidote gouge), the pressure solution (dissolution-precipitation) will be too slow relative to gouge deformation dominated by granular flow and rearrangement (e.g. Figs. 10a and 11a). Particles will rotate and displace with this only possible if accompanied by dilation. Frictional stability at this temperature is dominated by the mineralogical intergranular response as either velocity-strengthening or velocity-neutral. At higher temperatures (i.e., $T = 200$–300 °*C* for epidote gouge), pressure solution effects strengthen and gouge compaction counters the tendency for dilation apparent at lower temperatures. The fault gouge dilation rate depends on the displacement and porosity (and grain size/shape through packing). Increasing the shear velocity would result in elevated gouge porosity at a new steady state—contributing to a decreased dilation angle, reduction in frictional strength and resulting in the observed velocity-weakening behavior over a velocity-up-step. At further increased temperatures (i.e., $T = 400$ and 500 °*C* for epidote gouge), particle-particle pressure solution (dissolution-precipitation) is then sufficiently strong to dominate gouge deformation with the development of porosity suppressed (as observed in the denser and less porous structure in Figs. 10d-e and 11e-f) - with fault response returning to velocity-strengthening behavior (Bos and Spiers, 2002; Niemeijer and Spiers, 2006). In summary, fault instability ($a - b < 0$) at different temperatures primarily occurs due to

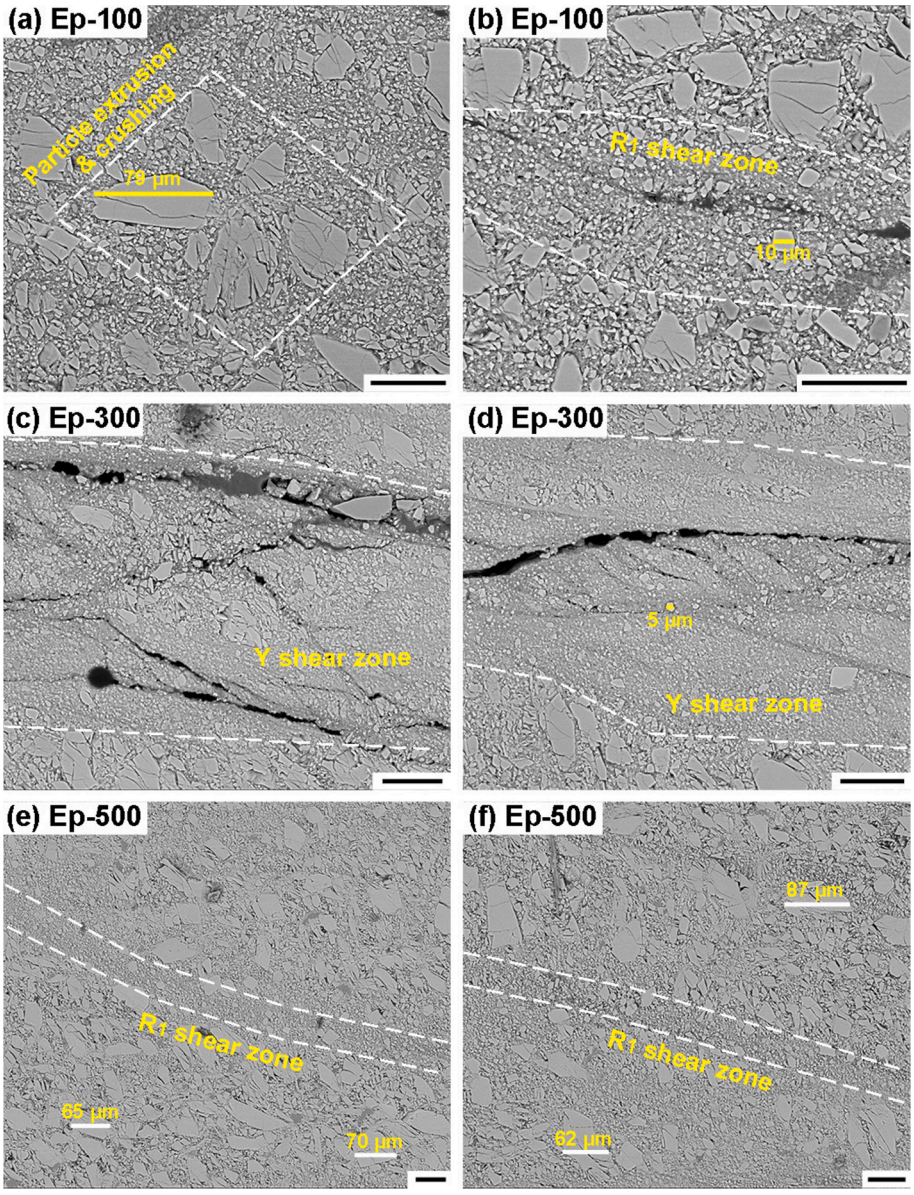

Fig. 11. Zoom-in backscattered microstructural images of the deformed gouges from Fig. 10, with (a)-(b), (c)-(d), and (e)-(f) from the experiments Ep-100, Ep-300 and Ep-500, respectively. Scale bars, 50 μm.

the competition between the granular flow-induced gouge dilation (i.e., the slip-dependent dilation) and pressure solution-induced gouge compaction (i.e., time-dependent compaction) (Chen and Spiers, 2016; Niemeijer and Spiers, 2006, 2007; Rutter and Mainprice, 1979).

At 300 °C, epidote instability is also influenced by effective normal stresses or elevated pore fluid pressures (Figs. 8–9), with the evolution in deformation mechanisms potentially interpreted as the competition between granular flow-induced gouge dilation and pressure solution-induced gouge compaction. Decreasing the effective normal stress is equivalent to lowering the gouge compaction rate driven by pressure solution. During shear, the gouge porosity would be increased at a lower effective normal stress after an upward velocity step—contributing to the much lower frictional strength observed after the velocity step and the enhanced velocity-weakening behavior observed at lower effective stresses. This is evident in the elevated gouge porosity of Fig. 12.

4.3. Implications for subduction fault stability under greenschist facies conditions

Our experimental results have important implications in understanding the stability of epidote-rich faults and the potential for a stability-instability-stability transition in subduction zones representative of greenschist metamorphism, with a conceptual fault zone model shown in Fig. 13 (Fagereng and Toy, 2011; Scholz, 1988, 2002; Sibson, 1983; Wehrens et al., 2016). We consider a typical geothermal gradient of 25 °C/km in warm subduction zones (Hyndman and Peacock, 2003) with the upper transition for velocity-strengthening to velocity-weakening occurring at a temperature of ~100 °C and a depth of 4 km, corresponding to the diagenetic zone. In this zone, epidote-rich faults exhibit velocity-strengthening behavior and primarily stable sliding – thus, deformation is dominated by particle-particle granular flow. Temperatures from ~100 °C to 300 °C bracket the seismogenic zone with epidote-rich faults showing velocity-weakening and stick-slip behaviors and promoting unstable sliding. Sub-greenschist metamorphic reactions could occur over this temperature range with

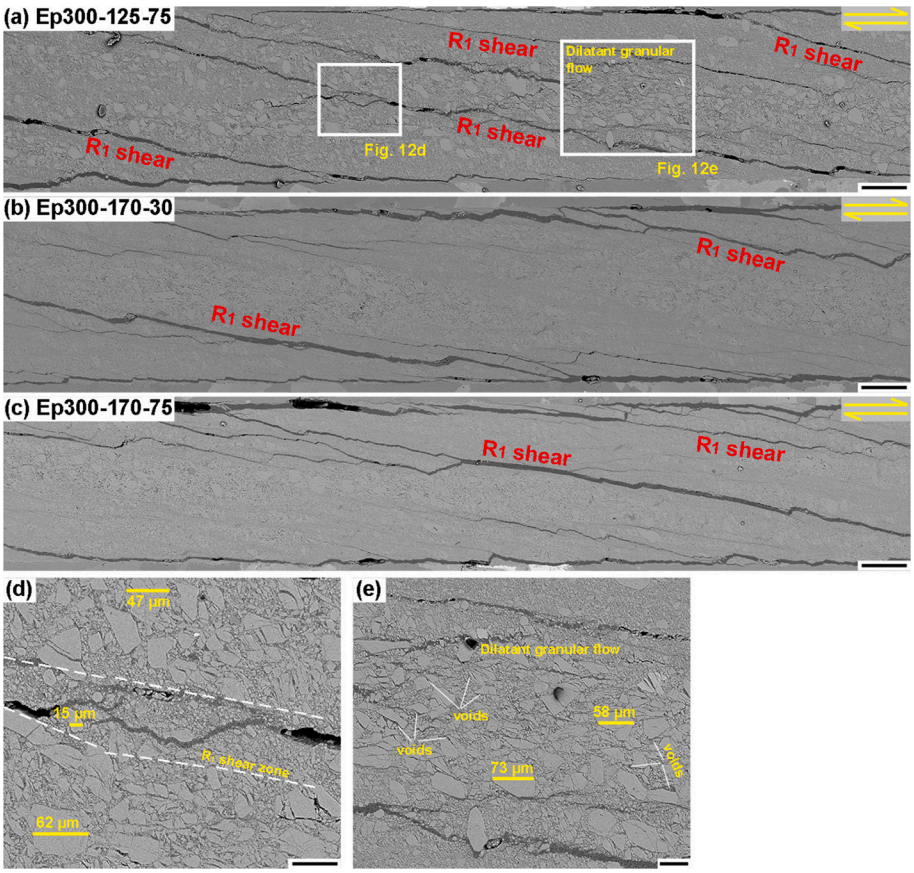

Fig. 12. Backscattered microstructural images of the deformed gouges at $T = 300\ ^{\circ}C$ but different pressures, (a) Ep300–125-75, (b) Ep300–170-30, and (c) Ep300–170-75. The two white rectangles in panel (a) indicate the panels (d)-(e). Scale bars in (a)-(c), 200 μm. Scale bars in (c)-(d), 50 μm.

earthquake ruptures readily nucleating. Dominant fault deformation mechanisms here are particle-particle granular flow and pressure solution with fault stability determined by their competition and the stronger of the two behaviors. Under greenschist metamorphic conditions with temperatures >300–500 $^{\circ}C$ for depths to ~20 km, epidote-rich faults will show a transition from velocity-weakening to velocity-strengthening (frictional to viscous transition) and deform predominantly by aseismic creep. The dominant fault deformation mechanisms thus include pressure solution and dislocation creep, resulting in the evolution of mixed behaviors over this range of temperatures and stresses. The observed rate-and-state frictional stability ($a - b$) of epidote gouge supports this purported stability-instability-stability transition in subducting faults under greenschist facies.

The magnitudes of effective normal stress and pore fluid pressure are also vital in defining the stability of faults within the subducting slab and in supporting this stability-to-instability transition. Decreasing the effective normal stress and/or elevating the pore fluid pressure are both capable of destabilizing epidote-rich faults and combined with elevated temperatures can promote such a stability-to-instability transition, as shown in Figure13. This relies on the water released from the dehydration reactions of hydrous minerals being contained within the slab to reduce effective stresses and thereby destabilize fault sliding, with a seismic event as the outcome.

In addition, epidote is stable not only under greenschist facies conditions but also stable into lower blueschist facies (clinozoisite) and hence within the slow earthquake window (i.e., up to 500 $^{\circ}C$). Epidotites are found in an ancient subduction interfaces in the Dent Blanche Thrust (Alps) where transient brittle-ductile deformation patterns are observed (Angiboust et al., 2015). Consequently, our experimental results not only aid in understanding the stability-instability transition in greenschist facies, but also have implications for understanding slow earthquakes in subduction zones. Firstly, despite the wide range of temperatures and pressures studied, epidote is likely present at seismogenic depths in subduction zones exhibiting velocity-weakening response only at 100–300 $^{\circ}C$ (Fig. 7) (An et al., 2021). This frictional stability-instability transition is consistent with observed slow earthquakes in old and cold subduction zones, e.g., the Tohoku subducted slab hosting the 2011 Tohoku earthquake hypocenter at temperatures in the range 150–200 $^{\circ}C$ (Kato et al., 2012; Ito et al., 2015; Sawai et al., 2016). Secondly, at $T = 300\ ^{\circ}C$, enhanced velocity-weakening occurs when the pore fluid pressure is higher and the effective stress is lower (Figs. 8–9). The transition that leads ($a - b$) values being negative but close to zero (neutral) is a necessary condition for generating slow earthquakes (Shibazaki et al., 2010). But this phenomenon may occur at a much lower temperature for epidote gouge. The above results suggest that slow earthquakes might also be induced by the accumulation of epidotite gouge within cold subduction zones.

Finally, we acknowledge that our experiments may still have some deficiencies in recreating natural conditions representative of subducting faults subject to greenschist facies conditions. The particle size distribution of the natural fault gouge may be vastly different from that simulated, – with the grain size exerting an important control on rates of dissolution-precipitation creep and thus frictional behavior. Like many other experiments, the minimum velocities of our current experiments are still at least one order of magnitude higher than those in nature. Experiments on recovered natural fault gouges and/or at shear velocities approaching plate convergence rates cm/yr (10^{-4}–10^{-3} $\mu m/s$) could further help in recreating natural fault conditions (Brune et al., 1969; Wallace, 1970).

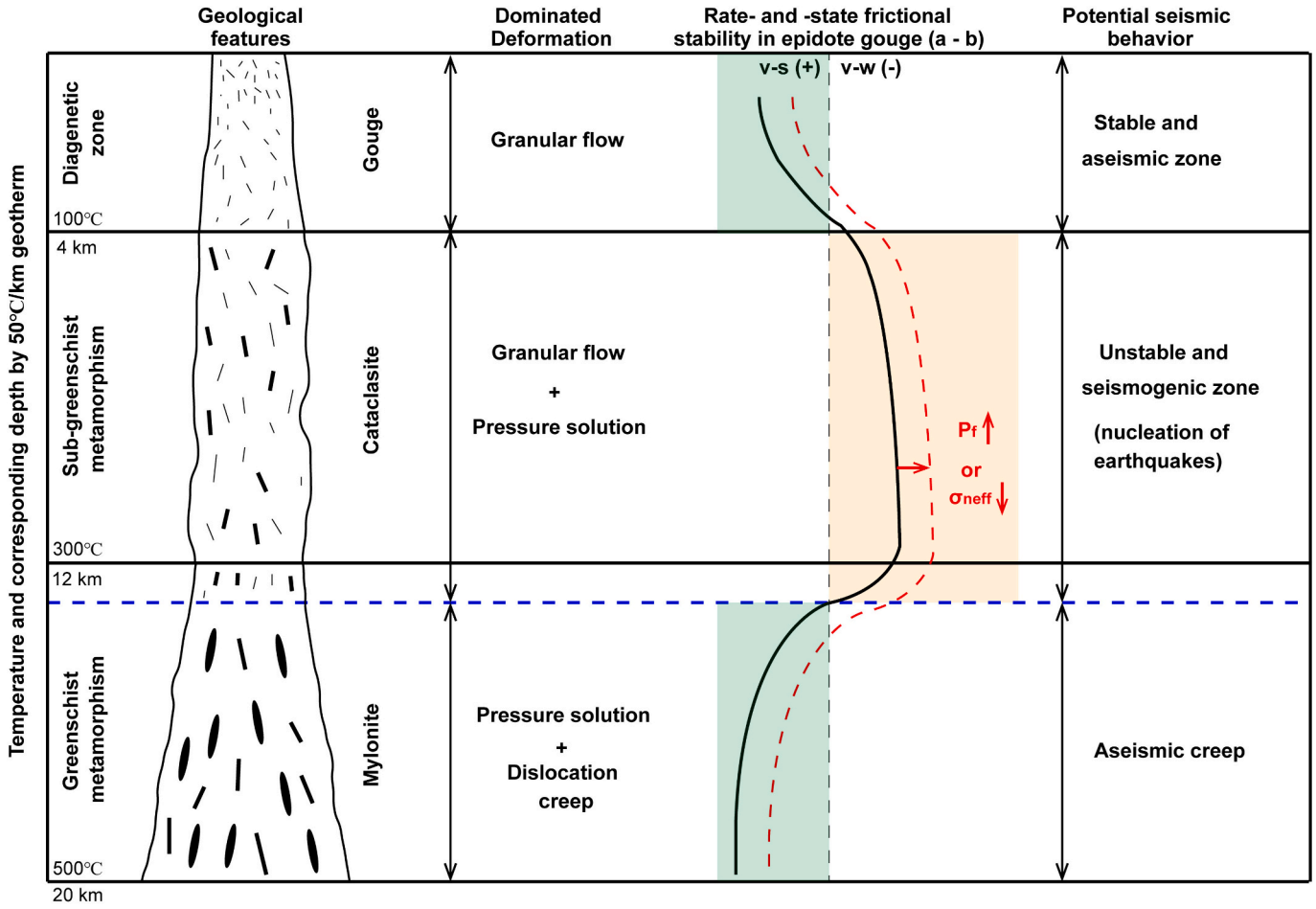

Fig. 13. Conceptual model of fault zone under greenschist metamorphic conditions based on the rate-and-state frictional stability behavior ($a - b$) of epidote gouge. Figure modified from Fagereng and Toy (2011), Scholz (1988, 2002) and Sibson (1983).

5. Conclusions

We use rate-and-state friction to separately explore the effects of elevated temperatures, elevated pore fluid pressures, and decreased effective normal stress on the frictional stability of epidote gouge. The results are then closely related to causal and contributing mechanisms of deformation and to explain the stability-instability-stability transition that occurs under greenschist facies subduction. The main conclusions of the study are as follows.

5.1. Temperature impact

Elevating the temperature has a negligible effect on the frictional strength ($\mu \sim 0.73$) of epidote gouge across our tested range but significantly affects frictional stability. With increasing temperature, the epidote gouge undergoes a transition from velocity-neutral behavior at $T = 100\,^{\circ}C$, to velocity-weakening and stick-slip behavior at $T = 200$ and $300\,^{\circ}C$, then back to velocity-strengthening behavior at $T = 400$ and $500\,^{\circ}C$.

Fluid Pressure Impact. The frictional strength of epidote gouge is only slightly affected by a variation in pore fluid pressure or effective normal stress. The elevated pore fluid pressure or the decreased effective normal stress both promote unstable slips in the epidote gouge.

5.2. Deformation mechanisms

Observed variations of the frictional stability of epidote gouge at different temperatures and pressures may be explained by a transition in deformation mechanisms from granular flow to pressure solution and dislocation creep. Competition between gouge dilation induced by the granular flow and gouge compaction induced by the pressure solution plausibly contributes to the observed velocity-weakening behavior. At higher temperatures, increased effective stresses and pore fluid pressures each promote gouge pressure solution rate and impact stability.

5.3. Fault stability-instability-stability transition

Our experimental results on the rate-and-state frictional stability of epidote gouge support a stability-instability-stability transition of epidote-filled faults under greenschist metamorphic conditions. The first transition from the velocity-strengthening to velocity-weakening response indicates the upper level of the seismogenic zone with the other transition from velocity-weakening to velocity-strengthening corresponding to the instability to stability transition, at depth.

CRediT authorship contribution statement

Mengke An: Writing – original draft, Methodology, Conceptualization. **Zhenyu Yin:** Writing – review & editing, Data curation. **Fengshou Zhang:** Writing – review & editing, Data curation. **Rui Huang:** Writing – review & editing, Data curation. **Derek Elsworth:** Writing – review & editing, Methodology.

Declaration of competing interest

We declare that we have no conflict of interest.

Data availability

Data will be made available on request.

Acknowledgement

This research is funded by the National Natural Science Foundation of China (42107163, 42320104003). DE acknowledges the support from the G. Albert Shoemaker endowment. We thank insightful suggestions from the editor Samuel Angiboust and two reviewers André Niemeijer & Brett Carpenter that contributed to significantly improve the manuscript.

Appendix A. Supplementary data

Supplementary data to this article can be found online at https://doi.org/10.1016/j.tecto.2024.230497.

References

An, M., Zhang, F., Min, K.-B., Elsworth, D., Marone, C., He, C., 2021. The potential for low-grade metamorphism to facilitate fault instability in a geothermal reservoir. Geophys. Res. Lett. 48, e2021GL093552 https://doi.org/10.1029/2021GL093552.

Ando, R., Takeda, N., Yamashita, T., 2012. Propagation dynamics of seismic and aseismic slip governed by fault heterogeneity and Newtonian rheology. J. Geophys. Res. Solid Earth 117 (B11), B11308. https://doi.org/10.1029/2012jb009532.

Angiboust, S., Kirsch, J., Oncken, O., Glodny, J., Monié, P., Rybacki, E., 2015. Probing the transition between seismically coupled and decoupled segments along an ancient subduction interface. Geochem. Geophys. Geosyst. 16 (6), 1905–1922. https://doi.org/10.1002/2015GC005776.

Apted, M.J., Liou, J., 1983. Phase relations among greenschist, epidote-amphibolite, and amphibolite in a basaltic system. Am. J. Sci. 283, 328–354.

Behr, W.M., Kotowski, A.J., Ashley, K.T., 2018. Dehydration-induced rheological heterogeneity and the deep tremor source in warm subduction zones. Geology 46 (5), 475–478. https://doi.org/10.1130/G40105.1.

Belzer, B.D., French, M.E., 2022. Frictional constitutive behavior of chlorite at low shearing rates and hydrothermal conditions. Tectonophysics 837, 229435. https://doi.org/10.1016/j.tecto.2022.229435.

Bird, D.K., Spieler, A.R., 2004. Epidote in geothermal systems. Rev. Mineral. Geochem. 56, 235–300. https://doi.org/10.2138/gsrmg.56.1.235.

Blanpied, M.L., Lockner, D.A., Byerlee, J.D., 1995. Frictional slip of granite at hydrothermal conditions. J. Geophys. Res. 100 (B7), 13,045–13,064. https://doi.org/10.1029/95JB00862.

Boneh, Y., Hirth, M.P.G., 2023. High-pressure mechanical properties of talc: Implications for fault strength and slip processes. J. Geophys. Res. Solid Earth 128 (3), e2022JB025815. https://doi.org/10.1029/2022JB025815.

Bos, B., Spiers, C.J., 2002. Frictional-viscous flow of phyllosilicate-bearing fault rock: microphysical model and implications for crustal strength profiles. J. Geophy. Res.: Solid Eath 107 (B2). https://doi.org/10.1029/2001JB000301. ECV 1-1-ECV 1-13.

Boulton, C., Moore, D.E., Lockner, D.A., Toy, V.G., Townend, J., Sutherland, R., 2014. Frictional properties of exhumed fault gouges in DFDP-1 cores, Alpine Fault, New Zealand. Geophys. Res. Lett. 41, 356–362. https://doi.org/10.1002/2013GL058236.

Brace, W.F., Byerlee, J.D., 1966. Stick-slip as a mechanism for earthquakes. Science 153 (3739), 990–992. https://doi.org/10.1126/science.153.3739.990.

Brantut, N., Schubnel, A., Guéguen, Y., 2011a. Damage and rupture dynamics at the brittle-ductile transition: the case of gypsum. J. Geophys. Res. 116, B01404 https://doi.org/10.1029/2010JB007675.

Brantut, N., Han, R., Shimamoto, T., Findling, N., Schubnel, A., 2011b. Fast slip with inhibited temperature rise due to mineral dehydration: evidence from experiments on gypsum. Geology 39 (1), 59–62. https://doi.org/10.1130/G31424.1.

Brantut, N., Schubnel, A., David, E.C., Héripré, E., Guéguen, Y., Dimanov, A., 2012. Dehydration-induced damage and deformation in gypsum and implications for subduction zone processes. J. Geophys. Res. 117, B03205 https://doi.org/10.1029/2011JB008730.

Brune, J.N., Henyey, T.L., Roy, R.F., 1969. Heat flow, stress, and rate of slip along the San Andreas Fault, California. J. Geophys. Res. 74 (15), 3821–3827. https://doi.org/10.1029/JB074i015p03821.

Chen, A.P., Yang, J.J., Zhong, D.L., Shi, Y.H., Liu, J.B., 2019. Epidote spherulites and radial euhedral epidote aggregates in a greenschist facies metavolcanic breccia hosting an UHP eclogite in Dabieshan (China): Implication for dynamic metamorphism. Am. Mineral. 104 (8), 1197–1212. https://doi.org/10.2138/am-2019-6980.

Chen, S., Spiers, C.J., 2016. Rate and state frictional and healing behavior of carbonate fault gouge explained using microphysical model. J. Geophys. Res. Solid Earth 121 (12), 8642–8665. https://doi.org/10.1002/2016JB013470.

Deseta, N., Andersen, T.B., Ashwal, L.D., 2014. A weakening mechanism for intermediate-depth seismicity? Detailed petrographic and microtextural observations from blueschist facies pseudotachylytes, Cape Corse, Corsica. Tectonophysics 610, 138–149. https://doi.org/10.1016/j.tecto.2013.11.007.

Diener, J.F.A., Fagereng, Å., Thomas, S.A.J., 2016. Mid-crustal shear zone development under retrograde conditions: pressure-temperature-fluid constraints from the Kuckaus Mylonite zone, Namibia. Solid Earth 7, 1331–1347. https://doi.org/10.5194/se-7-1331-2016.

Dieterich, J.H., 1979. Modeling of rock friction: 1. Experimental results and constitutive equations. J. Geophys. Res. 84 (B5), 2161. https://doi.org/10.1029/JB084iB05p02161.

Enami, M., Liou, J.G., Mattinson, C.G., 2004. Epidote minerals in high P/T metamorphic terranes: Subduction zone and high- to ultrahigh-pressure metamorphism. Rev. Mineral. Geochem. 56 (1), 347–398. https://doi.org/10.2138/gsrmg.56.1.347.

Fagereng, Å., Diener, J.F.A., 2011. San Andreas Fault tremor and retrograde metamorphism. Geophys. Res. Lett. 38, L23303 https://doi.org/10.1029/2011GL049550.

Fagereng, Å., Ikari, M.J., 2020. Low-temperature frictional characteristics of chlorite-epidote-amphibole assemblages: Implications for strength and seismic style of retrograde fault zones. J. Geophys. Res. Solid Earth 125, e2020JB019487. https://doi.org/10.1029/2020JB019487.

Fagereng, Å., Toy, V.G., 2011. Geology of the earthquake source: an introduction. Geological Society, London 359, 1–16. https://doi.org/10.1144/SP359.1.

Fang, Y., Elsworth, D., Wang, C., Jia, Y., 2018. Mineralogical controls on frictional strength, stability, and shear permeability evolution of fractures. J. Geophys. Res. Solid Earth 123 (5), 3549–3563. https://doi.org/10.1029/2017JB015338.

Forneris, J.F., Holloway, J.R., 2003. Phase equilibria in subducting basaltic crust: Implications for H_2O release from the slab. Earth Planet. Sci. Lett. 214 (1–2), 187–201. https://doi.org/10.1016/S0012-821X(03)00305-4.

Franz, G., Liebscher, A., 2004. Physical and chemical properties of the epidote minerals-An introduction. Rev. Mineral. Geochem. 56 (1), 1–81. https://doi.org/10.2138/gsrmg.56.1.1.

Frei, D., Liebscher, A., Franz, G., Dulski, P., 2004. Trace element geochemistry of epidote minerals. Rev. Mineral. Geochem. 56 (1), 553–605. https://doi.org/10.2138/gsrmg.56.1.553.

Giorgetti, C., Carpenter, B.M., Collettini, C., 2015. Frictional behavior of talc-calcite mixtures. J. Geophys. Res. Solid Earth 120, 6614–6633. https://doi.org/10.1002/2015JB011970.

Green II, H.W., Houston, H., 1995. The mechanics of deep earthquakes. Annu. Rev. Earth Planet. Sci. 23, 169–213. https://doi.org/10.1146/annurev.ea.23.050195.001125.

Gu, J.-C., Rice, J.R., Ruina, A.L., Tse, S.T., 1984. Slip motion and stability of a single degree of freedom elastic system with rate and state dependent friction. J. Mech. Phys. Solids 32 (3), 167–196. https://doi.org/10.1016/0022-5096(84)90007-3.

Hacker, B.R., Peacock, S.M., Abers, G.A., Holloway, S.D., 2003. Subduction factory 2. Are intermediate-depth earthquakes in subducting slabs linked to metamorphic dehydration reactions? J. Geophys. Res. Solid Earth 108 (B1). https://doi.org/10.1029/2001JB001129.

den Hartog, S.A.M., Spiers, C.J., 2013. Influence of subduction zone conditions and gouge composition on frictional slip stability of megathrust faults. Tectonophysics 600, 75–90. https://doi.org/10.1016/j.tecto.2012.11.006.

den Hartog, S.A.M., Spiers, C.J., 2014. A microphysical model for fault gouge friction applied to subduction megathrusts. J. Geophys. Res. Solid Earth 119, 1510–1529. https://doi.org/10.1002/2013JB010580.

den Hartog, S.A.M., Niemeijer, A.R., Spiers, C.J., 2012. New constraints on megathrust slip stability under subduction zone P–T conditions. Earth Planet. Sci. Lett. 353-354, 240–252. https://doi.org/10.1016/j.epsl.2012.08.022.

He, C., Yao, W., Wang, Z., Zhou, Y., 2006. Strength and stability of frictional sliding of gabbro gouge at elevated temperatures. Tectonophysics 427 (1–4), 217–229. https://doi.org/10.1016/j.tecto.2006.05.023.

He, C., Luo, L., Hao, Q.-M., Zhou, Y., 2013. Velocity-weakening behavior of plagioclase and pyroxene gouges and stabilizing effect of small amounts of quartz under hydrothermal conditions. J. Geophys. Res. Solid Earth 118 (7), 3408–3430. https://doi.org/10.1002/jgrb.50280.

Hu, H., Dai, L., Li, H., Hui, K., Sun, W., 2017. Influence of dehydration on the electrical conductivity of epidote and implications for high-conductivity anomalies in subduction zones. J. Geophys. Res. Solid Earth 122 (4), 2751–2762. https://doi.org/10.1002/2016JB013767.

Hyndman, R.D., Peacock, S.M., 2003. Serpentinization of the forearc mantle. Earth Planet. Sci. Lett. 212, 417–432. https://doi.org/10.1016/S0012-821X(03)00263-2.

Ikari, M.J., Saffer, D.M., Marone, C., 2009. Frictional and hydrologic properties of clay-rich fault gouge. J. Geophys. Res. 114, B05409 https://doi.org/10.1029/2008JB006089.

Im, K., Elsworth, D., Marone, C., Leeman, J., 2017. The impact of frictional healing on stick-slip recurrence interval and stress drop: implications for earthquake scaling. J. Geophys. Res. Solid Earth 122 (12), 10102–10117. https://doi.org/10.1002/2017JB014476.

Incel, S., Hilairet, N., Labrousse, L., John, T., Deldicque, D., Ferrand, T., Wang, Y., Renner, J., Morales, L., Schubnel, A., 2017. Laboratory earthquakes triggered during eclogitization of lawsonite-bearing blueschist. Earth Planet. Sci. Lett. 459, 320–331. https://doi.org/10.1016/j.epsl.2016.11.047.

Ito, Y., Hino, R., Suzuki, S., Kaneda, Y., 2015. Episodic tremor and slip near the Japan Trench prior to the 2011 Tohoku-Oki earthquake. Geophys. Res. Lett. 42, 1725–1731. https://doi.org/10.1002/2014GL062986.

John, T., Medvedev, S., Rüpke, L.H., Andersen, T.B., Podladchikov, Y.Y., Austrheim, H., 2009. Generation of intermediate-depth earthquakes by self-localizing thermal runaway. Nat. Geosci. 2, 137–140. https://doi.org/10.1038/ngeo419.

Jung, H., Green II, H.W., Dobrzhinetskaya, L.F., 2004. Intermediate-depth earthquake faulting by dehydration embrittlement with negative volume change. Nature 428, 545–549. https://doi.org/10.1038/nature02412.

Kalinowski, B.E., Faith-Ell, C., Schweda, P., 1998. Dissolution kinetics and alteration of epidote in acidic solutions at 25°C. Chem. Geol. 151 (1–4), 181–197. https://doi.org/10.1016/S0009-2541(98)00079-5.
Kato, A., Obara, K., Igarashi, T., Tsuruoka, H., Nakagawa, S., Hirata, N., 2012. Propagation of slow slip leading up to the 2011 M_W 9.0 Tohoku-Oki earthquake. Science 335, 705–708. https://doi.org/10.1029/95RG00353.
Kirby, S., 1995. Interslab earthquakes and phase changes in subducting lithosphere. Rev. Geophys. 33 (S1), 287–297. https://doi.org/10.1029/95RG00353.
Kolawole, F., Johnston, C.S., Morgan, C.B., Chang, J.C., Marfurt, K.J., Lockner, D.A., Reches, Z., Carpenter, B.M., 2019. The susceptibility of Oklahoma's basement to seismic reactivation. Nat. Geosci. 12, 839–844. https://doi.org/10.1038/s41561-019-0440-5.
Li, B., Xu, J., Zhang, D., Ye, Z., Huang, S., Fan, D., Zhou, W., Xie, H., 2021. Thermoelasticity and stability of natural epidote at high pressure and high temperature: implications for water transport during cold slab subduction. Geosci. Front. 12, 921–928. https://doi.org/10.1016/j.gsf.2020.05.022.
Liu, Y., He, C., 2020. Friction properties of hornblende and implications for slow-slip events in subduction zones. Tectonophysics 796, 228644. https://doi.org/10.1016/j.tecto.2020.228644.
Logan, J.M., Dengo, C.A., Higgs, N.G., Wang, Z.Z., 1992. Fabrics of experimental fault zones: Their development and relationship to mechanical behavior. In: Evans, B., Wong, T.-F. (Eds.), Fault Mechanics and Transport Properties of Rocks. Academic Press, New York, pp. 33–67. https://doi.org/10.1016/S0074-6142(08)62814-4.
Marieni, C., Voigt, M.J., Oelkers, E.H., 2021. Experimental study of epidote dissolution rates from pH 2 to 11 and temperatures from 25 to 200 °C. Geochim. Cosmochim. Acta 294, 70–88. https://doi.org/10.1016/j.gca.2020.11.015.
Marone, C., 1998. Laboratory-derived friction laws and their application to seismic faulting. Annu. Rev. Earth Planet. Sci. 26 (1), 643–696. https://doi.org/10.1146/annurev.earth.26.1.643.
Moore, D.E., Lockner, D.A., 2008. Talc friction in the temperature range 25°-400 °C: Relevance for fault-zone weakening. Tectonophysics 449 (1–4), 120–132. https://doi.org/10.1016/j.tecto.2007.11.039.
Moore, D.E., Lockner, D.A., 2011. Frictional strengths of talc-serpentine and talc-quartz mixtures. J. Geophys. Res. Solid Earth 116 (B1). https://doi.org/10.1029/2010JB007881.
Niemeijer, A.R., Collettini, C., 2014. Frictional properties of a low-angle normal fault under in situ conditions: thermally-activated velocity weakening. Pure Appl. Geophys. 171 (10), 2641–2664. https://doi.org/10.1007/s00024-013-0759-6.
Niemeijer, A.R., Spiers, C.J., 2006. Velocity dependence of strength and healing behaviour in simulated phyllosilicate-bearing fault gouge. Tectonophysics 427 (1–4), 231–253. https://doi.org/10.1016/j.tecto.2006.03.048.
Niemeijer, A.R., Spiers, C.J., 2007. A microphysical model for strong velocity weakening in phyllosilicate-bearing fault gouges. J. Geophys. Res. 112, B10405 https://doi.org/10.1029/2007JB005008.
Niemeijer, A.R., Boulton, C., Toy, V.G., Townend, J., Sutherland, R., 2016. Large-displacement, hydrothermal frictional properties of DFDP-1 fault rocks, Alpine Fault, New Zealand: implications for deep rupture propagation. J. Geophys. Res. Solid Earth 121 (2), 624–647. https://doi.org/10.1002/2015JB012593.
Okamoto, A.S., Verberne, B.A., Niemeijer, A.R., Takahashi, M., Shimizu, I., Ueda, T., Spiers, C.J., 2019. Frictional properties of simulated chlorite gouge at hydrothermal conditions: implications for subduction megathrusts. J. Geophys. Res. Solid Earth 124 (5), 4545–4565. https://doi.org/10.1029/2018JB017205.
Oliver, N.H.S., 1996. Review and classification of structural controls on fluid flow during regional metamorphism. J. Metamorph. Geol. 14 (4), 477–492. https://doi.org/10.1046/j.1525-1314.1996.00347.x.
Pawley, A.R., Redfern, S.A.T., Holland, T.J.B., 1996. Volume behavior of hydrous minerals at high pressure and temperature; I. thermal expansion of lawsonite, zoisite, clinozoisite, and diaspore. Am. Mineral. 81 (3–4), 335–340. https://doi.org/10.2138/am-1996-3-407.
Peacock, S.M., Hyndman, R.D., 1999. Hydrous minerals in the mantle wedge and the maximum depth of subduction thrust earthquakes. Geophys. Res. Lett. 26 (16), 2517–2520. https://doi.org/10.1029/1999GL900558.
Poli, S., Schmidt, M.W., 2004. Experimental subsolidus studies on epidote minerals. Rev. Mineral. Geochem. 56 (1), 171–195. https://doi.org/10.2138/gsrmg.56.1.171.
Raleigh, C.B., 1967. Tectonic implications of serpentinite weakening. Geophys. J. Int. 14 (1–4), 113–118. https://doi.org/10.1111/j.1365-246X.1967.tb06229.x.
Reinen, R.A., Weeks, J.D., Tullis, T.E., 1994. The frictional behavior of lizardite and antigorite serpentinites: experiments, constitutive models, and implications for natural faults. Pure Appl. Geophys. 143, 317–358. https://doi.org/10.1007/BF00874334.
Rice, J.R., 1983. Constitutive relations for fault slip and earthquake instabilities. Pure Appl. Geophys. 121, 443–475.
Rice, J.R., Ruina, A.L., 1983. Stability of steady frictional slipping. J. Appl. Mech. 50 (2), 343–349. https://doi.org/10.1115/1.3167042.
Rose, N.M., 1991. Dissolution rates of prehnite, epidote, and albite. Geochim. Cosmochim. Acta 55 (11), 3273–3286. https://doi.org/10.1016/0016-7037(91)90488-Q.
Ruina, A., 1983. Slip instability and state variable friction laws. J. Geophys. Res. Solid Earth 88 (B12), 10,359–10,370. https://doi.org/10.1029/JB088iB12p10359.
Rutter, E.H., Mainprice, D.H., 1979. On the possibility of slow fault slip controlled by a diffusive mass transfer process. Gerlands Beitr. Geophysik 88 (2), 154–162.
Sawai, M., Niemeijer, A.R., Plümper, O., Hirose, T., Spiers, C.J., 2016. Nucleation of frictional instability caused by fluid pressurization in subducted blueschist. Geophys. Res. Lett. 43 (6), 2543–2551. https://doi.org/10.1002/2015GL067569.
Schmidt, M.W., Poli, S., 1998. Experimentally based water budgets for dehydrating slabs and consequences for arc magma generation. Earth Planet. Sci. Lett. 163 (1–4), 361–379. https://doi.org/10.1016/S0012-821X(98)00142-3.
Scholz, C.H., 1988. The brittle-plastic transition and the depth of seismic faulting. Geol. Rundsch. 77, 319–328.
Scholz, C.H., 2002. The Mechanics of Earthquakes and Faulting, 2nd edn. Cambridge University Press, Cambridge.
Shibazaki, B., Bu, S., Matsuzawa, T., Hirose, H., 2010. Modeling the activity of short-term slow slip events along deep subduction interfaces beneath Shikoku, Southwest Japan. J. Geophys. Res. Solid Earth 115 (B4), B00A19. https://doi.org/10.1029/2008JB006057.
Sibson, R.H., 1983. Continental fault structure and the shallow earthquake source. J. Geol. Soc. Lond. 140, 741–767. https://doi.org/10.1144/gsjgs.140.5.0741.
Spandler, C., Hermann, J., Arculus, R., Mavrogenes, J., 2003. Redistribution of trace elements during prograde metamorphism from lawsonite blueschist to eclogite facies; implications for deep subduction-zone processes. Contrib. Mineral. Petrol. 146, 205–222. https://doi.org/10.1007/s00410-003-0495-5.
Spinelli, G.A., Wang, K., 2009. Links between fluid circulation, temperature, and metamorphism in subducting slabs. Geophys. Res. Lett. 36, L13302 https://doi.org/10.1029/2009GL038706.
Tesei, T., Harbord, C.W.A., De Paola, N., Collettini, C., Viti, C., 2018. Friction of mineralogically controlled serpentinites and implications for fault weakness. J. Geophys. Res. Solid Earth 123 (8), 6976–6991. https://doi.org/10.1029/2018JB016058.
Tian, P., He, C., 2019. Velocity weakening of simulated augite gouge at hydrothermal conditions: Implications for frictional slip of pyroxene-bearing mafic lower crust. J. Geophys. Res. Solid Earth 124, 6428–6451. https://doi.org/10.1029/2018JB016456.
Tulley, C.J., Fagereng, Å., Ujiie, K., Diener, J.F.A., Harris, C., 2022. Embrittlement within viscous shear zones across the base of the subduction thrust seismogenic zone. Geochem. Geophys. Geosyst. 23 (8), e2021GC010208 https://doi.org/10.1029/2021GC010208.
Verberne, B.A., Niemeijer, A.R., De Bresser, J.H.P., Spiers, C.J., 2015. Mechanical behavior and microstructure of simulated calcite fault gouge sheared at 20-600°C: Implications for natural faults in limestones. J. Geophys. Res. Solid Earth 120, 8169–8196. https://doi.org/10.1002/2015JB012292.
Wallace, R.E., 1970. Earthquake recurrence intervals on the San Andreas Fault. Geol. Soc. Am. Bull. 81 (10), 2875–2890. https://doi.org/10.1130/0016-7606(1970)81[2875:ERIOTS]2.0.CO;2.
Wehrens, P., Berger, A., Peters, M., Spillmann, T., Herwegh, M., 2016. Deformation at the frictional-viscous transition: evidence for cycles of fluid-assisted embrittlement and ductile deformation in the granitoid crust. Tectonophysics 693, 66–84. https://doi.org/10.1016/j.tecto.2016.10.022.
Zhang, F., Huang, R., An, M., Min, K.-B., Elsworth, D., Hofmann, H., Wang, X., 2022. Competing controls of effective stress variation and chloritization on friction and stability of faults in granite: implications for seismicity triggered by fluid injection. J. Geophys. Res. Solid Earth 127 (8), e2022JB024310. https://doi.org/10.1029/2022JB024310.